Applied Geography 58 (2015) 65–83

Contents lists available at ScienceDirect

Applied Geography

journal homepage: www.elsevier.com/locate/apgeog

Localising deformation along the elevation of linear structures: An experiment with space-borne InSAR and RTK GPS on the Roman Aqueducts in Rome, Italy

Deodato Tapete [a, *], Stefano Morelli [b], Riccardo Fanti [b], Nicola Casagli [b]

[a] Department of Geography, Institute of Hazard, Risk and Resilience (IHRR), Durham University, Lower Mountjoy, South Road, DH1 3LE Durham, UK
[b] Department of Earth Sciences, University of Firenze, Via G. La Pira 4, 50121 Firenze, Italy

ARTICLE INFO

Article history:
Available online

Keywords:
Persistent Scatterer Interferometry
GPS
RADARSAT
Deformation
Structural monitoring
Rome

ABSTRACT

We map and monitor the condition of linear structures using Measurement Points (MPs) from satellite Interferometric Synthetic Aperture Radar (InSAR), and deal with the uncertainty of localising the detected deformation along the building elevation. We combine spatial information of the MPs with elevation measurements collected by Real Time Kinematic (RTK) GPS surveying to understand where structural motions occurred. The MPs are geolocated along the z-direction by exploiting their height information (h_{MP}) compared to the elevation of the surveyed buildings and surrounding ground (h_{GPS}). This approach aims to find a good compromise between the required accuracy and repeatability, and the advantages of reduced time-consumption and cost-effectiveness offered by RTK GPS. Reliability of the method is proved via the experiment on the Roman Aqueducts in the southern peri-urban quarters of the city of Rome, Italy. We focus on the linear man-made structures of the ancient to modern aqueduct systems. These are challenging anthropogenic features to monitor with InSAR due to their huge extent, variety of condition and architectural complexity. Of the total 13,519 MPs retrieved from SqueeSAR™ processing of 87 RADARSAT-1 Fine Beam Mode 3 ascending scenes (2003–2010), the MPs spatially attributed to the local linear features and the surroundings are analysed with regard to: (i) their densities against building type, structure planimetric orientation and vegetation coverage; and (ii) their height distribution against RTK GPS micro-topographic surveying in seven sample areas. Numerical analysis of h_{MP}–h_{GPS} pairs result in high correlation (R^2 equals 0.970), and their cross-comparison allows validation of 3D geolocation of the MPs, also demonstrating the usefulness of complementary surveying by laser distance meter device whenever RTK GPS is not feasible. Cross-referenced h_{MP} values are then used to reclassify the MPs and generate final map products to support the design of in-situ inspection activities. We discuss beneficial impacts for condition monitoring and assessment at the scale of single building through the examples of the medieval tower Torre del Fiscale and the Roman arcades of the Claudian Aqueduct. The MP height information improves the understanding of the deformation estimates, and also contributes to address hazard mitigation measures and restorations.

Introduction

Building surveying in urban areas is among the fields of geographical application that has benefitted greatly from the advent of new remote sensing technologies from space and their increasing use in the last decade (Mcnally & Mckenzie, 2011; Sever, 2000), in addition to the well established aerial photography and free-access imagery from optical satellites (e.g., Google Earth). Applications at the scale of single building included, but were not limited to: cadastre updating (e.g., Ali, Tuladhar, & Zevenbergen, 2012), identification of urban features (e.g., Bhaskaran, Paramananda, & Ramnarayan, 2010), assessment of urban sprawl (e.g., Jat, Garg, & Khare, 2008; Xu & Min, 2013), and damage mapping in emergency contexts (e.g., Dong, Li, Dou, &Wang, 2011; Witharana, Civco, & Meyer, 2013). As found in affine geographical sciences such as land cover change detection and mapping (Liu &

* Corresponding author. Tel.: +44 (0) 191 33 41867; fax: +44 (0) 191 33 41801.
E-mail addresses: deodato.tapete@durham.ac.uk, deodato.tapete@gmail.com (D. Tapete), stefano.morelli@unifi.it (S. Morelli), riccardo.fanti@unifi.it (R. Fanti), nicola.casagli@unifi.it (N. Casagli).

http://dx.doi.org/10.1016/j.apgeog.2015.01.009

Yang, 2015 among the latest research), key factors that make these Earth Observation technologies highly advantageous compared with traditional surveying methods are the cost-effectiveness and reduced time-consumption.

Such aspects are nowadays of high concern for individual surveyors, as well as authorities in charge of built environment management. Professionals and technical officers seek for sustainable solutions to undertake ordinary activities of building inspection, in a period when reduced human resources and funds allocated are being drastically reduced due to financial cuts and economic constraints (cf., for instance, English Heritage, 2011 and Cecchi & Gasparoli, 2010, 2011, with specific regard to English and Italian current contexts). This also aligns with recommendations at international level, including those proposed by the European Parliament (2007) and recalled in the European Commission decision (2013/743/EU) in the framework of the Horizon 2020 initiative. The current trend is indeed to encourage the development of feasible methods of surveying, data collection and mapping in GIS environment to support cultural heritage monitoring and damage assessment.

There is recent literature demonstrating that satellite Interferometric Synthetic Aperture Radar (InSAR) ground motion data from multi-interferogram processing can help building surveyors, heritage conservators and geographers to achieve this purpose. Persistent Scatterer Interferometry (PSI; Crosetto, Monserrat, Jungner, & Crippa, 2009) in particular is suitable to monitor the condition of buildings, man-made structures and infrastructure (e.g., Bianchini et al., 2014; Bock, Wdowinski, Ferretti, Novali, & Fumagalli, 2012; Cigna, Del Ventisette, et al., 2012a; Kourkouli, Strozzi, & Wegmuller, 2012; Parcharidis, Foumelis, Kourkouli, & Wegmuller, 2009a). It was also proved valuable for diagnostic investigation in historical urban and rural sites (Cigna, Lasaponara, Masini, Milillo, & Tapete, 2014; Iadanza et al., 2013; Parcharidis, Foumelis, Pavlopoulos, & Kourkouli, 2009b; Pratesi, Tapete, Terenzi, Del Ventisette, & Moretti, 2015; Tapete & Cigna, 2012a, 2012b), in a way that allows early detection of surface deformation as indicator of structural instability of the building and/or instability of foundations and underlying bedrock (Tapete, Fanti, Cecchi, Petrangeli, & Casagli, 2012).

The spatial dimension of this type of analysis relates to understanding where the deformation that has been recorded in the satellite time series occurs. To this scope in this paper we combine satellite InSAR data from PSI processing with topographic measurements by GPS surveying, to solve the uncertainty related to the spatial interpretation of the geolocation information associated to deformation patterns.

PSI-based condition assessment relies specifically on the provision of sparse grid of Measurement Points (MPs) with associated time series of surface deformation which allows (1) distinction of stable and unstable areas, (2) analysis of the temporal evolution of deformation and (3) recognition of deformation trends.

Among the spatial properties of each MP, we stress in this paper the importance of the height information. Some studies have paid attention to this parameter, mainly to: better identify the object(s) on the ground (e.g., Perissin & Ferretti, 2007); map topographic changes of urban features (e.g., Delgado Blasco, Hendrickx, De Laet, Verstraeten, & Hanssen, 2012); geolocate precisely MPs via the aid of LiDAR Digital Surface Models (DSM) with regard to buildings and infrastructure under sinkhole risk (Chang & Hanssen, 2014).

By using the MP height we want to identify the object the MP deformation estimate refers to. If the MP is spatially located over a building, we aim to define the architectural component/portion of the object investigated that is subject to deformation (the latter depending on the spatial resolution of SAR imagery, i.e. the extent to which the SAR sensor is capable to spatially resolve two neighbouring elements on the ground).

Answers to the above questions are specifically sought by surveyors of linear structures (e.g., viaducts, aqueducts, colonnades, terraced buildings), the elevation of which predominates with respect to the other two dimensions. Location within urban, peri-urban and rural areas can be challenging, since the proximity of unrelated objects (e.g., light poles) can cause difficulty to the spatial attribution of the identified MPs. Consequently, deformation patterns can be misinterpreted, with detriment to the reliability of PSI results.

To address this practical issue, we explored the feasibility of using Real Time Kinematic (RTK) GPS (Featherstone & Stewart, 2001; Hofmann-Wellenhof, Lichtenegger, & Collins, 2001) to survey samples of a wider region of interest (ROI) and solve the 3D geolocation of the MPs, taking advantage of the good compromise between reduced time-consumption, accuracy, cost-effectiveness and flexibility offered by RTK GPS surveying technique (Morelli, Segoni, Manzo, Ermini, & Catani, 2012; Morelli et al., 2014). We tested the method in the southern quarters of the city of Rome, Italy, owing to its variety of urban layout and landscape, focusing on the kilometre-long aqueduct system which dates back to Roman up to modern times. The choice of this test site allows us to demonstrate the sustainability of the method we propose, thereby offering an alternative to the traditional approaches of regular monitoring (e.g., visual inspections and in-situ spot measurements) to deal with huge ROIs. We spatially investigated PSI data obtained from multi-interferogram processing of 7-year long C-band RADARSAT-1 Fine Beam Mode 3 imagery by means of SqueeSAR™ algorithm (Ferretti et al., 2011).

Section 'Methodology' describes how to exploit PSI height information by combining the GIS-based preliminary assessment of the MPs with RTK GPS and ancillary topographic measurements. We also illustrate how surveyors and geographers can use this combined spatial information to feed into mapping products. Land cover characteristics and features of the study area are then introduced, alongside the technical parameters of the RADARSAT-1 data. Reliability and effectiveness of the method is demonstrated via the discussion of the experiment we undertook in Southern Rome. The final mapping product summarising the outcomes of the sample survey is presented in Section 'Results and discussion', followed by selected examples of linear features and historical structures to discuss the benefits that can be achieved for condition assessment of building environment and heritage assets.

Methodology

Flowchart in Fig. 1 illustrates the methodological approach that we implemented, mainly consisting of the following phases:

1. GIS-based data integration and preliminary assessment (Fig. 1a);
2. Topographic survey with in-situ elevation measurements by RTK GPS (Fig. 1b), coupled with complementary surveys (Fig. 1c) whenever physical obstacles, logistics constraints, conservation needs and/or safety issues limit the accessibility for object geolocation with RTK GPS;
3. Deformation analysis and condition assessment (Fig. 1d and e).

GIS-based data integration and preliminary assessment

The sparse grids of MPs that are obtained from the PSI processing of a sufficiently long time series (at least 15–20 images in the case of C-band SAR imagery acquired with monthly frequency from the same satellite and geometry) are handled in a GIS environment (Fig. 2) and spatially analysed by using the following properties:

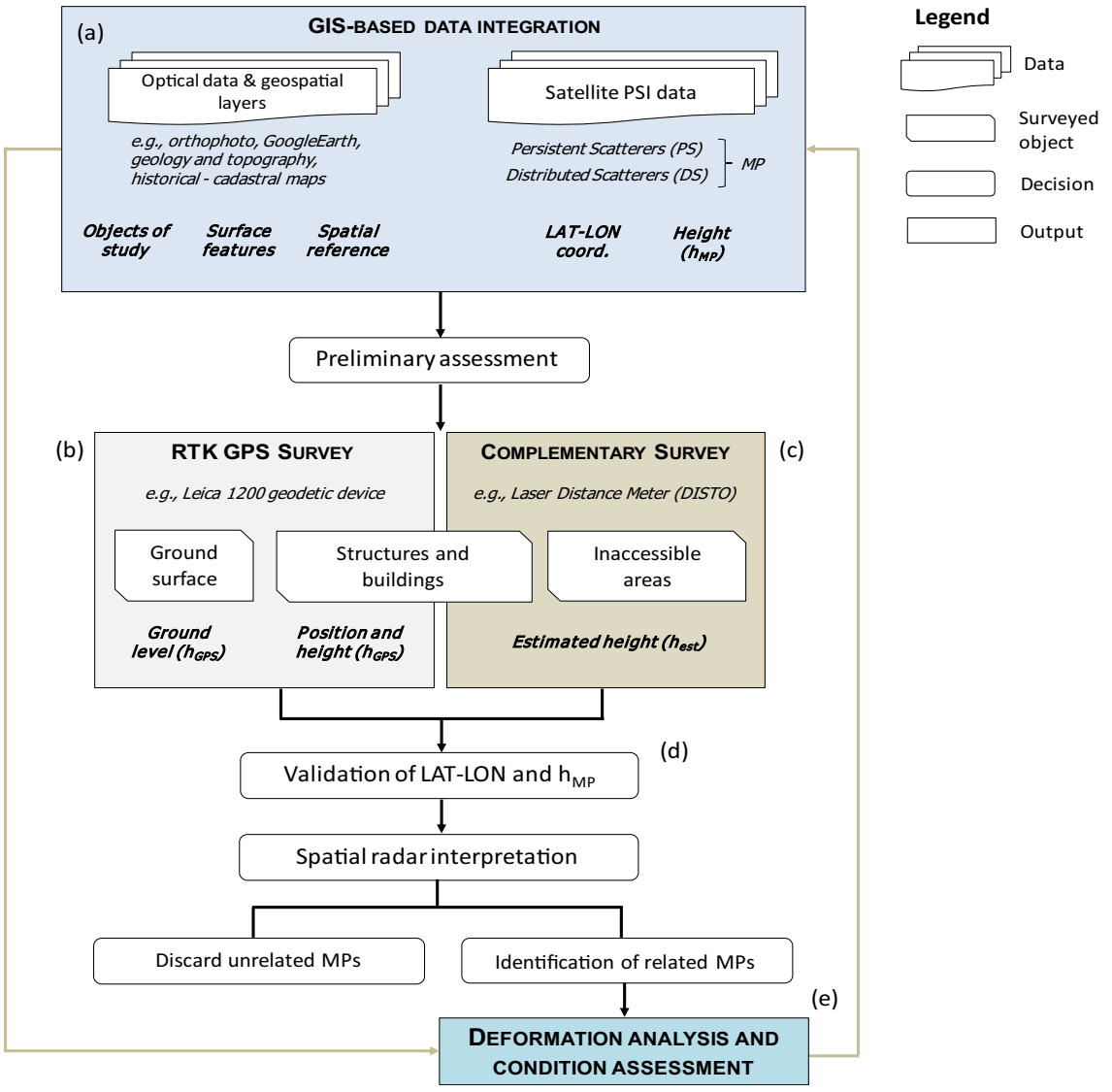

Fig. 1. Flowchart of the PSI – RTK GPS methodology proposed and implemented in this paper.

– *Latitude and longitude coordinates* (LAT and LON) of the point used as physical representation of the identified MP;
– *Height* (h_{MP}) as ellipsoidic elevation of the physical point that is determined with regard to the WGS84 reference system, and associated standard deviation (SD_{hMP}) [both expressed in metres].

PSI data are integrated with geospatial layers containing background information related to: historical records of past collapses, deterioration processes (e.g., subsidence, block detachment), human-induced transformations in time (e.g., restorations, renovations, change of use, demolition and rebuilding) that have affected the surveyed buildings. The temporal proximity between the last acquisition of the PSI time series and the date of production of the cartographic reference (e.g., orthophoto, cadastral map, building inventory) is highly recommended, to reduce uncertainty in spatial interpretation of the MPs.

The output of this initial step is a first map product zoning where the deformation patterns are preliminarily associated to the objects on the ground based on the multi-layering with the cartographic reference and the ancillary data.

It is worth noting that the 3D geolocation accuracy of the MPs might need to be improved prior to the interpretation of the ground motion data. Fig. 2 shows, for instance, the MP geolocation shift observed between the 2008 orthophoto used for georeferencing and the higher resolution 2011 Virtual Earth over two sample areas in the ROI. Erroneous overlapping onto the Virtual Earth image is clearly detectable for isolated linear features based on the spatial distribution pattern of the MPs (Fig. 2b and c), whilst it is less obvious in densely built-up areas (Fig. 2d and e). Such shift can be corrected at an early stage of the interpretation by using, for instance, the approach described in Bateson et al. (2012).

As recently recalled by Chang and Hanssen (2014), the precision achievable for positioning MPs that are retrieved from InSAR processing of medium resolution C-band SAR imagery such as ERS and ENVISAT archives (ground resolution ~20–30 m) is of the order of 1 m. Of the same magnitude (about 1 m) is the interferometric uncertainty of the vertical positioning of MPs.

As discussed later in the paper (see Section 'Results and discussion'; cf. Fig. 7a), by processing RADARSAT-1 Fine Beam Mode 3 PSI data, resulting SD_{hMP} values span from 1 to 1.5 m, and this can make a significant difference when the operator has to attribute a

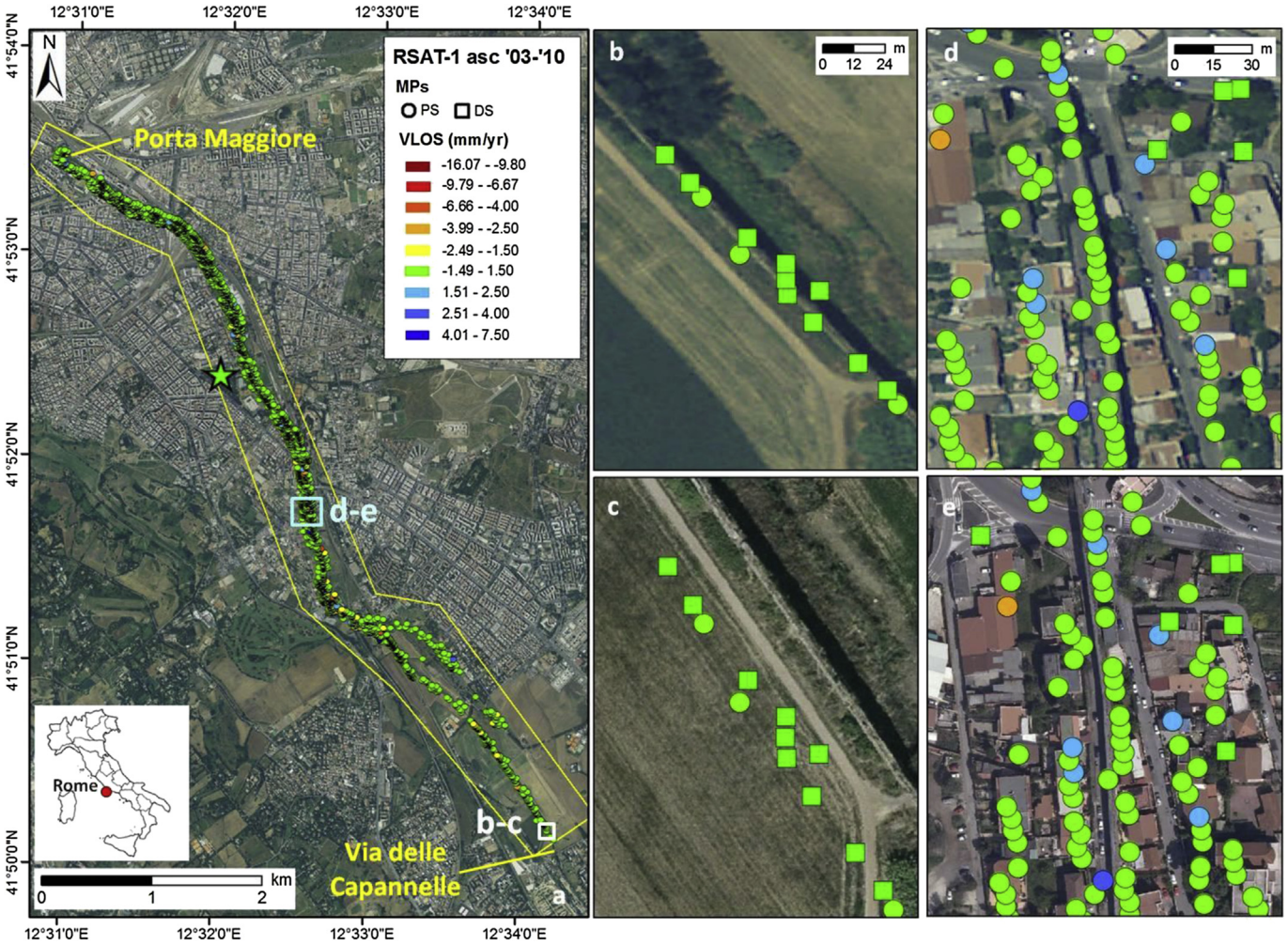

Fig. 2. a) RADARSAT-1 F3 ascending MPs (2003–2010) from SqueeSAR™ processing over the ROI (yellow polygon) of Southern Rome, Italy, which are spatially associated with the linear features and surrounding environment. Zoomed views of agricultural (b and c; white square in a) and densely urbanized (d and e; cyan rectangle in a) sectors show the issue of spatial interpretation due to the MP shift with regard to the visual reference, by comparing the 2008 orthophoto (PCN, 2014; used for georeferencing during the processing) and the Virtual Earth image, respectively. Green star in (a) indicates the location of the reference point for the processing. (For interpretation of the references to colour in this figure legend, the reader is referred to the web version of this article.)

spatial meaning to the h_{MP} values. Of course, these height values reflect the type of backscattering mechanisms involved in the SAR image capture, as well as the location at which the backscattering occurred (i.e. whether it happened: at the corner between the bottom of the structure and the surrounding ground surface or road pavement; at the top of the structure; or at the corner of a protruding architectural element). For the scope of monitoring the condition of buildings and linear features with relevant elevation, MP positioning along the z-direction means that we need to understand whether the deformation detected from satellite is due to instability of the foundations and/or the surrounding ground or, instead, it is an effect of intrinsic instability of the structure itself.

Topographic surveying

RTK GPS survey

This task is the core of the methodological approach and aims to collect field micro-topographic measurements which are used to validate the spatial meaning of each h_{MP} value, i.e. to geolocate the identified MP with regard to the objects on the ground and the surrounding environment (Fig. 1b). Sample areas over which to carry out RTK GPS survey are selected following the preliminary assessment. The sampling needs to be statistically representative, and include both stable and unstable areas. This will act as a further control that the operator-driven radar interpretation is not biased or affected by sources of under-estimation.

The RTK GPS topographic survey is therefore conducted at the scale of single building or, in cases of complex and long linear features, at the scale of single architectural portion (e.g., crown or extrados of an aqueduct arch instead of the pier base). The elevation measurement is taken at the points where the deformation is supposed to have occurred or is being occurring based on the PSI data and their geolocation as observed with regard to the visual reference used within the GIS environment (cf. Fig. 2b–e).

The RTK GPS device can only record position (i.e. LAT and LON) and height (hereinafter indicated as h_{GPS}) of the surface above which the rover is positioned. Therefore position and h_{GPS} can be only obtained for those points that can be accessed (Fig. 3a), provided that sufficient visibility to more than four GPS satellites are achieved (Fig. 4). The latter condition is compulsory to acquire the ellipsoidic heights with centimetre error (less than 5 cm) and to avoid all the undesirable disturbance effects that the instrument software could not minimize.

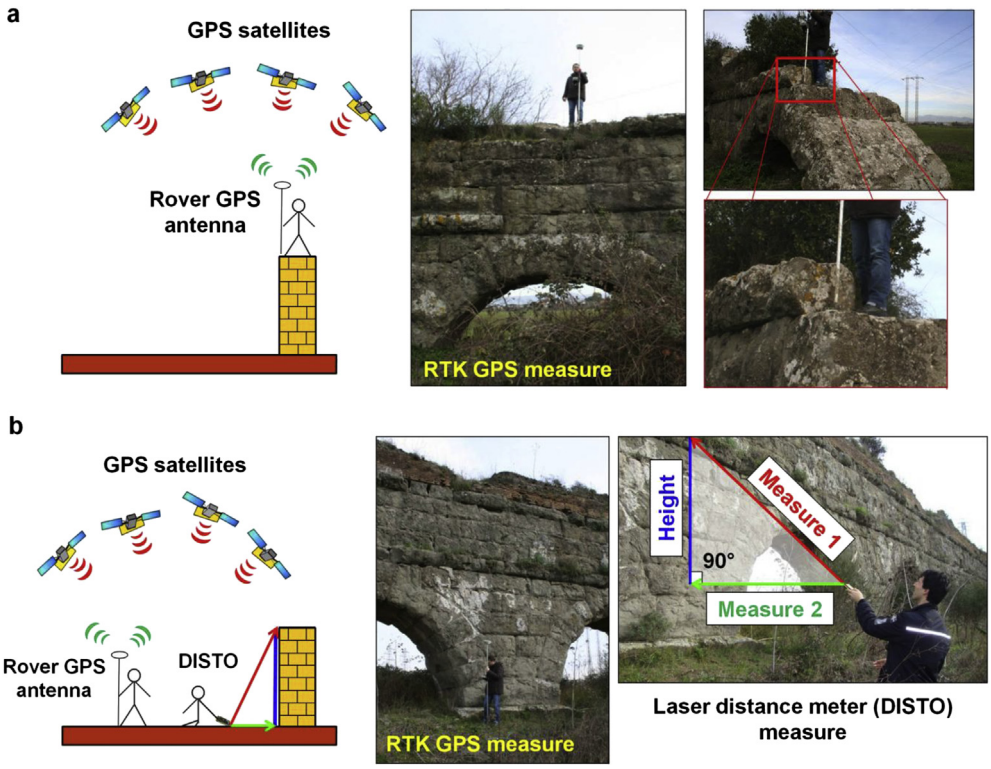

Fig. 3. a) Sketch of the RTK GPS survey (cf. Fig. 1b) showing how to collect h_{GPS} of the point of interest whenever it is directly accessible. b) Complementary survey by laser distance meter device (DISTO) is coupled with the collection of h_{GPS} of the ground level, to retrieve the estimated height (h_{est}) of the point of interest along the elevation of the building. Connection with a minimum of four satellites is always required for the GPS device.

The output of the RTK GPS survey consists of a sparse grid of points over both the ground surface and portions of buildings and structures, for which ground level, position and ellipsoid elevation (h_{GPS}) are collected. This dataset is then combined with LAT-LON and h_{MP} of the MPs for the purposes of validation and radar interpretation (cf. Section 'Validation and spatial radar interpretation').

In our survey we used a Leica 1200 geodetic device, with the following characteristics: i) fast satellite acquisition (about 5 s are sufficient for a correct registration); ii) high accuracy measurements by means of Carrier phase on L1: 0.2 mm rms, on L2: 0.2 mm rms and Code – pseudorange – on L1 and L2: 20 mm rms; iii) tracking to low elevations (the device acquires more than 99% of all possible observations above 10° elevation); iv) phase multipath mitigation technology thanks to SmartCheck algorithms; v) jamming resistant; vi), high up-date rate (selectable from 0.05 s -20Hz- to 60 s); vii) low latency (less than 0.03 s); viii) fast and reliable, long-range RTK (30 km range or more in favourable conditions, typically about 50 s needed to acquire all satellites after switching on and re-acquisition of satellites after "loss of lock", e.g. passing through tunnel, typically within 1 s). As being used as a RTK rover in differential mode, in our study area the real-time correction message (NRT) was received from the nearest reference station (i.e. Nearest Correction) belonging to the national network fully managed by Leica Geosystems Italia. This network, named SmartNet ItalPoS, is the first GNSS network with national coverage that

Fig. 4. Examples of a) enclosed spaces (e.g., aqueduct structures in Via del Mandrione, Rome) and b) physical obstacles (e.g., a tall tree close to the arcades of Felice Aqueduct in Vicolo dell'Acquedotto Felice, Rome) that can create practical difficulties to the collection of RTK GPS micro-topographic measurements.

provides services of real-time positioning and post-processing and it is set in the ETRF2000-RDN reference system currently used by the Italian Military Geographic Institute (IGMI).

Complementary laser distance meter survey

This complementary survey is added within the operational chain (Fig. 1c) to account for those situations when the GPS acquisition errors are too high, and the receiving antenna cannot establish good connection with satellites, or the considered object is not physically accessible and ancillary sources of information providing reliable elevation values (e.g., planimetric or isometric drawings) are not available.

In these circumstances, to situate our research in real-world context of the heritage sector and provide a cost-effective and sustainable surveying solution, we used a laser handheld distance meter device (in this case a Leica DISTO™ D5) to retrieve the height of structures, buildings and inaccessible objects, being aware of the error sources and approximation of this handy method (cf., for instance, Barkovic, Zrinjski, & Boric, 2013).

Fig. 3b demonstrates how to combine RTK GPS and DISTO measurements. The point of interest (e.g., the extrados top of an arch) is illuminated with the DISTO laser, and measures 1 and 2 coinciding with the sides of a right-angled triangle are acquired, by checking the angle calculation on the DISTO screen (Fig. 3b). The point height is then retrieved based on simple trigonometric functions as the elevation of the point from the ground surface (h_{DISTO}). Then the estimated height (h_{est}) of the point of interest is calculated as follows:

$$h_{est} = h_{GPS} + h_{DISTO} \quad (1)$$

where the major source of error is due to the operator's inaccuracy in taking measures 1 and 2. To reduce this unavoidable shortcoming, it is always recommended to repeat the h_{DISTO} measurement at least three times. The mean value can be accepted, if the difference between the repetitions is less than 0.1 m (which is appropriate given the scale of investigation and compared with the metre-level SD_{hMP}).

Although this method has intrinsic sources of error (anyway less than the metre-one provided with the PSI estimates) and is obviously coarser than RTK GPS, the discussion of the scatter plots reported in Section 'Results and discussion' (cf. Figs. 7 and 8) demonstrates that this method can be exploited as a valid alternative, provided that it is used only when other solutions are not doable and measurement repeatability is confirmed.

Validation and spatial radar interpretation

This decision process (Fig. 1d) is undertaken according to the namesake task described in Tapete and Cigna (2012b), and aims in this case to refine the MP spatial interpretation that was conducted at an early stage during the preliminary assessment. The surveyed h_{GPS} (or h_{est} for those cases where ancillary survey was required) is cross-compared with its corresponding h_{MP}, so that 3D geolocation of the MP is assessed without uncertainty and we can understand where the radar backscattering mechanism occurred and the MP was generated. The result of this task is therefore the spatial attribution of the MP to a specific portion of the object on the ground.

In this regard, MPs retrieved from medium resolution SAR time series are mostly geolocated at the bottom or atop of the man-made structure, dependently on the object shape, dimension and orientation with regard to the satellite acquisition geometry (cf. scatter plots in Figs. 7 and 8, and later discussion for aqueduct arcades).

Ground truth in the survey sample also serves to discard reliably unrelated MPs that might have been previously considered mistakenly in the radar mapping. It is worth noting that the difficulty in identification of unrelated MPs outside the survey areas based on height values tends to increase, as the urban environment surrounding the building of interest becomes more complex and various (cf. comparison between the rural area and urban sector reported in Fig. 2b–e).

Deformation analysis and condition assessment

Once the 3D location of the MPs is clarified, preliminarily assessed deformation patterns are classified as follows:

- '*Alarming*' – sectors of the ROI where deformation estimates take on values well higher than the stability threshold (e.g., $|V_{LOS}| > 1.5$ mm/yr in the case of C-band SAR imagery with monthly sampling), and show clear MP spatial distribution covering a significant portion up to the whole structure, as well as spatial correlation with local hazard factors. The identification of acceleration/trend inversion within the time series contributes to raise the alert level.
- '*Likely*' – sectors where deformation estimates would suggest a high level of alert, but the absence/scarcity of underpinning information or lack of evidence of spatial correlation with local hazard factors makes in-situ validation essential.
- '*Ambiguous*' – sectors where MPs show displacement rate within the stability threshold (e.g., $|V_{LOS}| < 1.5$ mm/yr), but trend changes are observed within the time series.
- '*Negligible*' – both MP parameters and geospatial layers do not highlight any specific issue.

The associated deformation estimate is analysed with respect to displacement trend and deviations that might have been recorded within the time series. This surface indicator is then used to assess the condition of the object on the ground, with specific regard to the temporal period covered by the processed SAR data stack.

Section 'Mapping patterns at small scale' shows how the deformation estimate can be fused together with the height information of the MPs, while Section 'Condition and damage assessment at large scale' demonstrates how the mapping product with deformation pattern classification can guide during in-situ application of PSI datasets to collect ground truth data and relate with the available background knowledge (i.e. the task of the geospatial analytical chain sketched in Fig. 1e). Moving from a small-scale mapping to large-scale investigation, selected examples reported therein also highlight the direct contribution of a correct spatial attribution of the deformation estimates to address recommendations for countermeasures to mitigate, or even prevent, damages to structures and infrastructure in the ROI.

Prolongation of monitoring activity is among the pursuable options, meaning that further archive or newly SAR acquisitions can be processed to extend the temporal coverage of satellite surveillance. This circumstance is accounted for in the flowchart in Fig. 1, as an iteration of the entire methodological procedure (see grey dashed line on the right side). It is worth mentioning here that, if new SAR images are added to the already processed data stack, it is possible that MPs obtained will not coincide with those retrieved from previous PSI processing. Hence, RTK GPS microtopography of the ROI could be partially re-used, while further in-situ measurements on sample areas might be needed. In the best scenario, the intermediate steps of the chain can be skipped and iteration will consist of a direct updating of the previous condition assessment (see grey dashed line on the left side in Fig. 1).

Study area and input data

Land cover and geologic setting of the linear archaeological systems in Southern Rome, Italy

We selected a huge portion of the building environment in the southern suburbs of Rome, Italy, outside of the ancient Aurelian Walls (Fig. 2a and 5). The ROI extends from Piazzale Labicano (Porta Maggiore; Fig. 6g) to Via delle Capannelle (Fig. 5 and 6d), with a total area of ~6.1 km^2. According to the GMES European Urban Atlas – IT001L – Roma 1:10,000 scale (EC, 2011), the land cover is mainly composed of the following classes: code 20000 agricultural + semi-natural areas (27.3% of the total area), 12100 industrial and commercial units (21.8%), 11100 continuous urban fabric (19.6%) and 11210 discontinuous dense urban fabric (12.3%). This assortment reflects the transformations due to the urban sprawl and requalification that were undertaken since 1950s, as also recently highlighted by Frondoni, Mollo, and Capotorti (2011). Therefore the entire ROI can be classified from rural to residential/commercial peri-urban moving from south to north, towards the city centre. Such variety of land cover makes this site suitable to assess the performance of PSI processing over both isolated fabric and man-made structures up to highly densely built-up quarters.

Furthermore, the ROI is well known for the archaeological ruins and monuments dating from Roman to Modern Age, among which we focus here on the Ancient Aqueducts (Fig. 6). The latter form a complex hydraulic network and are a palimpsest as result of subsequent building phases since the 3rd century BC, with alterations, additions and even demolitions, the most recent of which were produced in the second half of the 20th century. Differential condition is observed across the whole network, and the various sections of the aqueducts can be classified accordingly (cf. Table 2 and classification of building types and related statistics reported in Section 'Numerical analysis of MP distribution vs. object properties'). With the total linear length of ~10.9 km (nearly 7.5 km of which running across the ROI without any interruption, with a predominant NW–SE planimetric orientation; cf. Table 3), this aqueduct network is a demonstrative example of an architectural system with linear geometric configuration which extends over a huge area of investigation. The scale factor is indeed highly relevant in this context, because regular field inspections of condition assessment obviously require human efforts and facilities that are costly and even time-consuming. Therefore PSI techniques can be a feasible solution, provided that the uncertainty with regard to spatial and height information of the MPs are reliably solved.

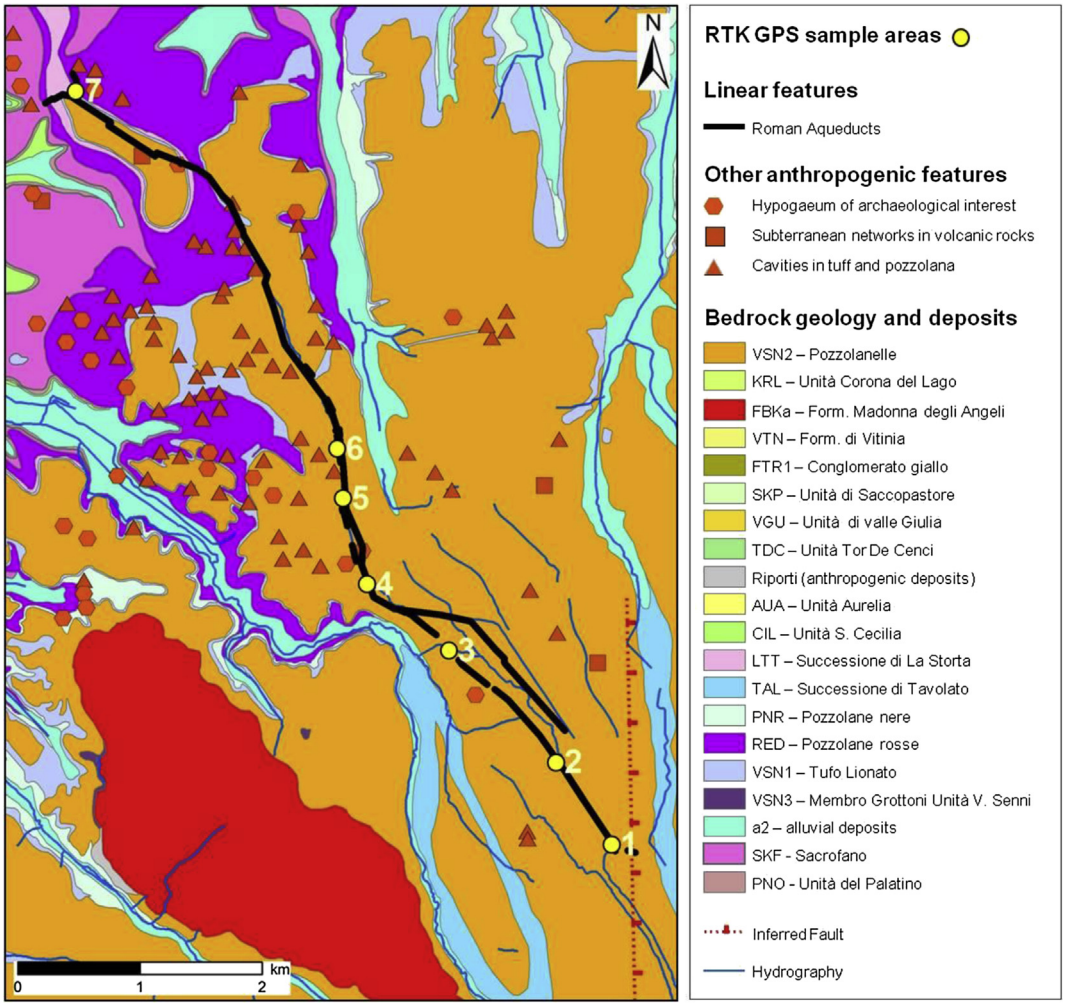

Fig. 5. Geological map of the ROI (cf. Fig. 2a) with indication of the linear and anthropogenic features. Numbered yellow points show the centroid location of the sample areas where RTK GPS and complementary surveys were carried out: 1) Aqua Claudia – Capannelle; 2) Aqua Claudia – Appio Claudio; 3) Aqua Claudia – railway; 4) Torre del Fiscale; 5) Felice Aqueduct – Vicolo dell'Acquedotto Felice; 6) Felice Aqueduct – Via Frascati; 7) Porta Maggiore. (For interpretation of the references to colour in this figure legend, the reader is referred to the web version of this article.)

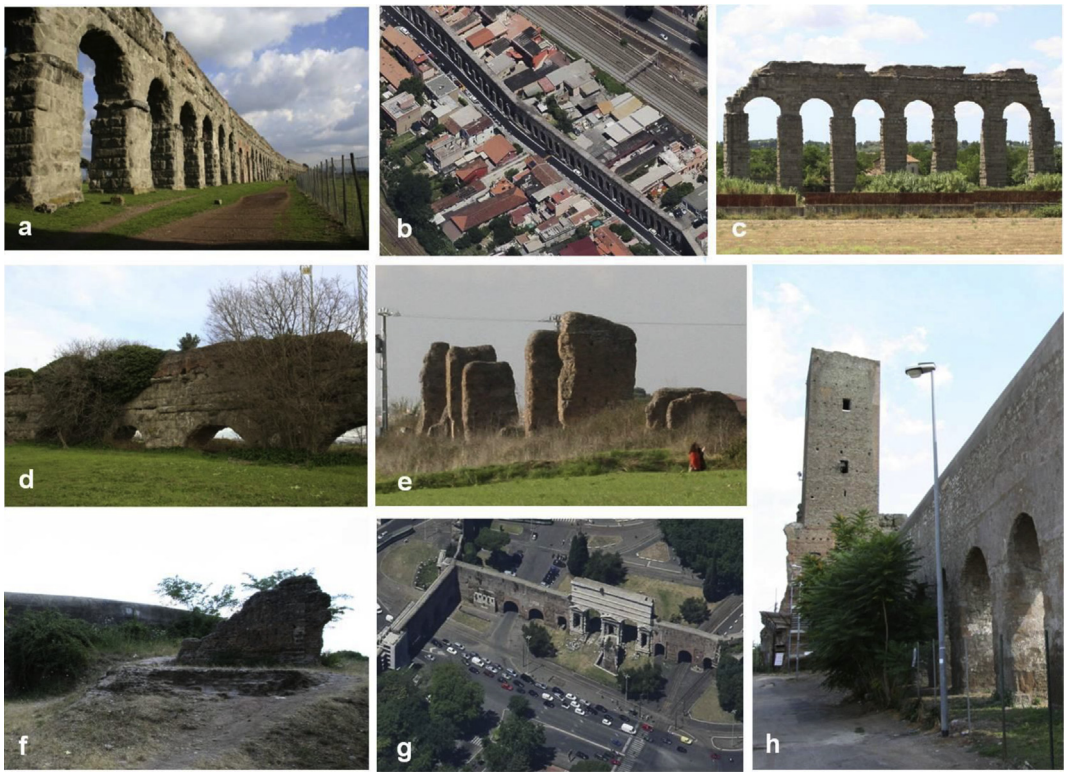

Fig. 6. Examples of building types across the ROI: a) arcades in agricultural fields/green areas; b) arcades within densely built-up areas; c) continuous arches with few and (d) dominant vegetation coverage; e) arch ruins; f) scatter; g) monumental gate; h) tower.

In regard to condition monitoring, all these monuments are chronically exposed to geohazards, due to the surrounding environment and the geological background (see Fig. 5). The latter is composed of superficial deposits (i.e. recent alluvial sediments mainly made of fine soils and anthropogenic deposits formed by the accumulation of heterogeneous materials for roads and railways embankments and fillings) which partially cover the subcropping bedrock composed of pyroclastic products emitted by the Colli Albani mafic caldera (Giordano et al., 2006; Karner, Marra, & Renne, 2001; Ventriglia, 1971, 2002; Vinkler, Cashman, Giordano, & Groppelli, 2012; Watkins, Giordano, Cas, & De Rita, 2002).

In particular, the predominant lithological units of the ROI are (Fig. 5):

(i) *Pozzolane Rosse* (RED) – a dark-red, massive and chaotic ignimbrite, emitted at 457 ± 4 ka likely related to a caldera collapse, generally 10–20 m thick, but up to 80 m thick, where ponded in paleovalleys. Its matrix is mostly made of coarse-ash shards, and crystal fragments of leucite, clinopyroxene and biotite;
(ii) *Tufo Lionato* (VSN1) – part of the *Villa Senni Eruption Unit* as sillar, lithoidal, and yellow to orange, to brown in a pyroclastic density current deposit. Its matrix is extensively zeolitised into chabasite and phillipsite;
(iii) *Pozzolanelle* (VSN2) – part of the *Villa Senni Eruption Unit* as a dark grey to dark red pyroclastic density current deposit, massive and chaotic, generally 20 m thick and up to 80 m thick in proximal areas. Differently from the *Tufo Lionato*, the *Pozzolanelle* is non-cemented and preserves its matrix supported texture. This is made of coarse-ash shards, and abundant crystal fragments of leucite, clinopyroxene and biotite.

Subterranean cavities, excavated over the centuries for different purposes (e.g., caves, catacombs, hydraulic burrows; Sciotti, 1982; Tapete et al., 2014, Tapete, Fratini, Mazzei, Cantisani, & Pecchioni, 2013; Ventriglia & Camponeschi, 1982), run across these lithological units, frequently in proximity of the archaeological ruins over the investigated ROI. Risk of areal collapses is well known (Comerci et al., 2012), and structural instability due to ground movements can add onto the surface deterioration effects due to vegetation growth, exposure to weathering and lack of regular maintenance.

RADARSAT-1 2003-2010 PSI input dataset

PSI processing was carried out over the whole ROI by Tele-Rilevamento Europa S.r.l. (TRE) within the partnership with the Department of Earth Sciences, University of Firenze, Italy, by using Local SqueeSAR™ analysis (Ferretti et al., 2011; TRE, 2010). The processed data stack included 87 RADARSAT-1 scenes (C-band, $\lambda = 5.6$ cm), which were acquired between 07/03/2003 and 22/02/2010 along ascending orbits in Fine Beam Mode 3 (F3), with sampling frequency nearly regularly equal to 24 days (i.e. the nominal satellite repeat cycle). Only a few occasional lacks are observed within the time series, in one occurrence up to 7 SAR images missed (i.e. between 06/02/2004 and 23/07/2004). The image acquired on 04/12/2006 was selected as master scene, with maximum temporal baseline of 1368 days (i.e. with regard to the first acquisition). The nominal ground-range resolution is around 8 m. It is worth noting here that, although the current X-band radar constellations (e.g., TerraSAR-X and COSMO-SkyMed) nowadays offer better resolution to perform deformation analyses at the scale of single building, for the scope of this research the RADARSAT-1 data stack was preferred owing to its longer temporal coverage over the 2000s.

The false alarm rate was fixed at 10^{-5} (Ferretti, Prati, & Rocca, 2001), while the reference point (coordinates LAT: 41.8737°, LON:

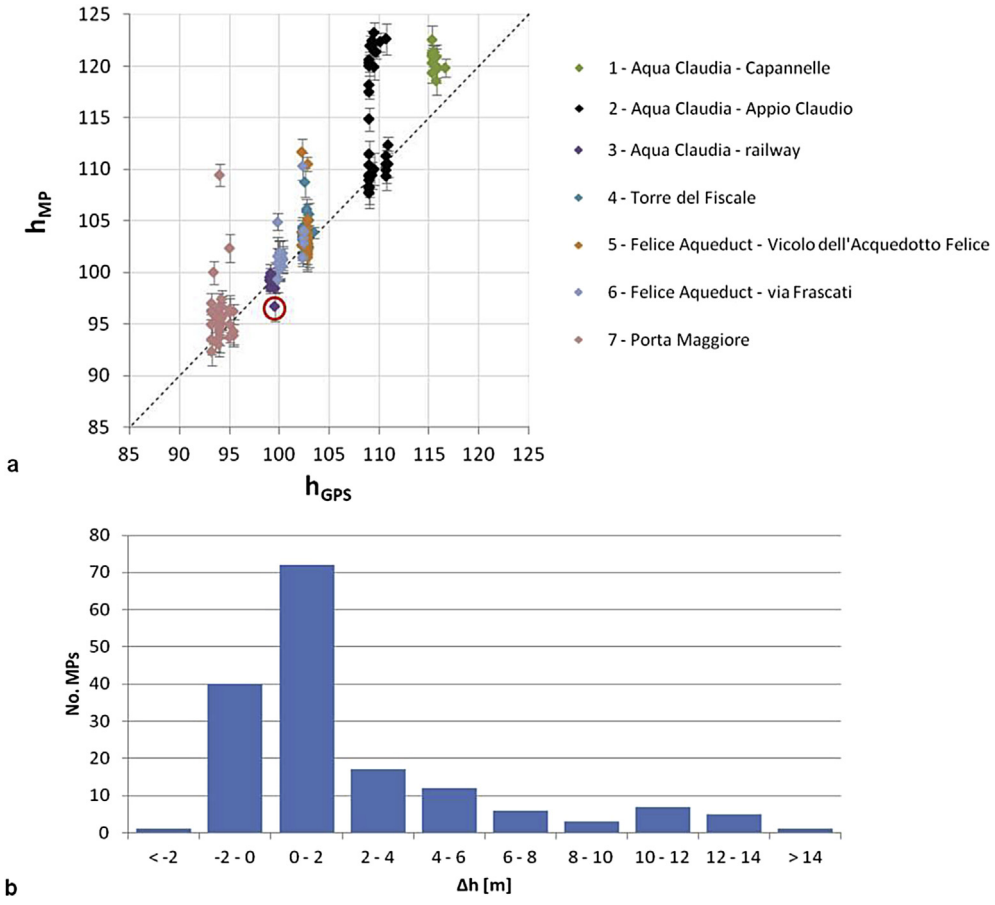

Fig. 7. a) Scatter plot of h_{MP} vs. h_{GPS} for the seven survey sample areas, and b) histogram of MP distribution with regard to Δh, i.e. $h_{MP} - h_{GPS}$, the latter being the RTK GPS measurement of the ground level.

12.5331°) was located in a stable area overlying VSN2 bedrock (Fig. 2a). The geospatial layer used for MP georeferencing was the 2008 UTM 33N orthophoto (Fig. 2), that was accessed via the WMS service of Portale Cartografico Nazionale (PCN, 2014). This orthophoto was also used for both the preliminary assessment and spatial radar interpretation, and therefore the shift issue shown in Fig. 2c and e for the Virtual Earth image was not of concern for the experiment.

Results and discussion

The discussion section moves through the analytical and mapping steps that the geographer needs to follow to localize the observed deformation, discriminate and map differential condition between building sectors and within each of them, and eventually identify the source of instability at large-scale investigation.

In particular the key steps are:

- understanding the nature of the MP dataset with regard to its spatial distribution over the ROI (Section 'Numerical analysis of MP distribution vs. object properties'). This is done via a numerical analysis of the spatial distribution of the retrieved MPs to explore the effect due to structure type and geometric properties (i.e. planimetric orientation), as well as of one of the most important environmental factors that can influence the MP identification, i.e. the vegetation coverage. This steps provide guidance for the selection of sample area and design of in-situ measurement campaign;
- accuracy assessment of the height measurements taken in the field by using both the surveying solutions we tested, i.e. RTK GPS and DISTO (Sections 'h_{MP} - h_{GPS} correlation' and 'RTK GPS and DISTO validation'). The scatter plots show how these two sets of height measurements can be effectively coupled with the respective h_{MP} values;
- generation of a mapping product fusing together the deformation and spatial location information (Section 'Mapping patterns at small scale') in preparation for large-scale investigation in sectors of interest that result as being affected by deformation (Section 'Condition and damage assessment at large scale').

Numerical analysis of MP distribution vs. object properties

Table 1 summarizes the results and related statistics obtained from the SqueeSAR™ processing.

As per the algorithm by Ferretti et al. (2011), our grid of MPs include 'Persistent Scatterers' (PS) as a result of point-wise deterministic object identification, and the so-called 'Distributed Scatterers' (DS).

Of the total 13,519 MPs identified over the ROI (Fig. 2a), 358 are the MPs that intersect the track and physical boundaries of the linear features of the ancient aqueducts and historical buildings, as per the GIS multi-layering with the 2008 orthophoto and the inventory of the monuments. This MP density accounts for the 2.6% of the MPs obtained from the SqueeSAR™ processing, with ~33 MPs per linear kilometre, which can be considered a relatively satisfactory output.

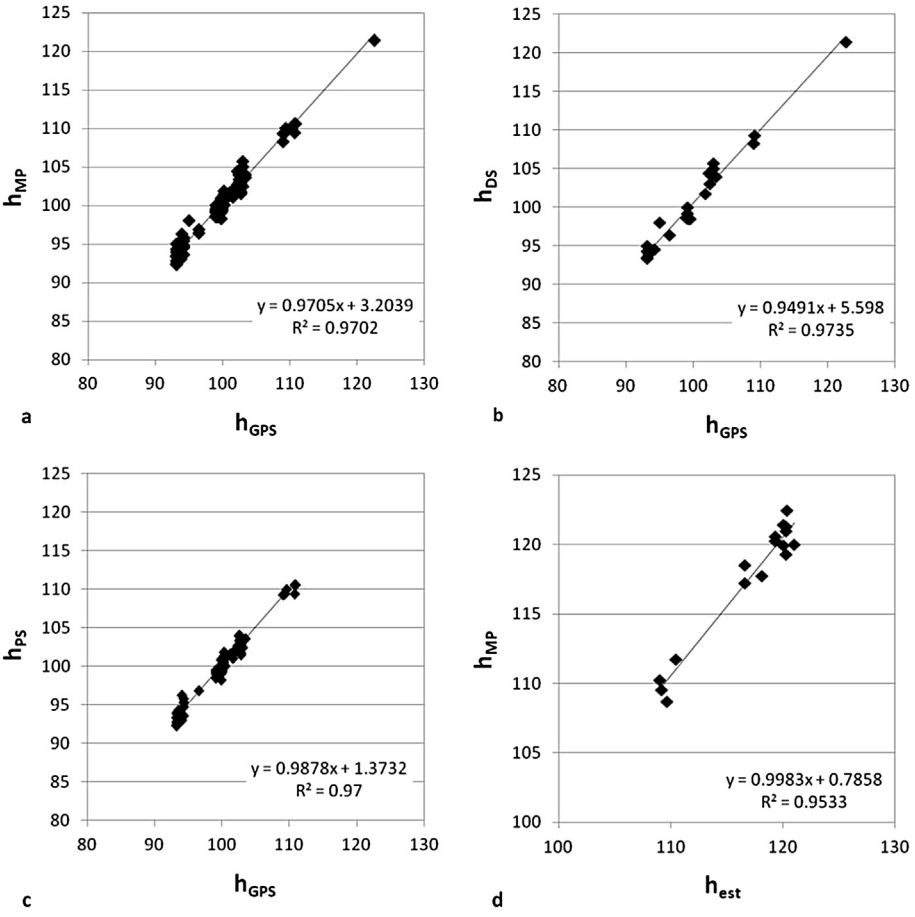

Fig. 8. Validation scatter plots comparing: a) h_{MP} vs. h_{GPS}; b) h_{DS} vs. h_{GPS}; c) h_{PS} vs. h_{GPS}; d) h_{MP} vs. h_{est}, for the seven survey sample areas.

This result needs to be assessed against the following three aspects that could have been detrimental:

(i) the reduced planimetric extent of the man-made structures investigated (the height significantly predominates with respect to the other two dimensions, with values up to 3–4 times the basal length as it happens, for instance, in the case of the medieval tower called 'Torre del Fiscale'; cf. Fig. 6h);
(ii) the vegetation coverage that in some cases inhibits the MP identification;
(iii) the object orientation compared to the satellite Line-Of-Sight (LOS) geometry which impacts on the visibility.

Despite the above, the PS/DS ratio over the linear features of ~1.8 means that PS nearly double the number of DS. This even improves the PS/DS ratio observed across the whole ROI (~1.6), most of which is covered by urban fabric and infrastructure (cf. statistics and comments on local land cover in Section 'Study area and input data').

Table 1
Summary of the MPs statistics over the ROI, linear features and the 10-m buffer zone which are retrieved from SqueeSAR™ processing of RADARSAT-1 F3 ascending imagery covering from 07/03/2003 to 22/02/2010.

Location	MPs	PS	DS	PS/DS
ROI	13,519	8372	5147	1.63
Linear features	358	232	126	1.84
10 m buffer zone	545	209	336	0.62
Linear features + 10 m buffer zone	903	441	462	0.95

Accounting for the fact that the structural health of buildings is also affected at some extent by the stability of the surrounding ground, a buffer zone of 10 m was defined and related statistics of MP spatial distribution were calculated (Table 1). It is worth mentioning here that the choice of the buffer size relates with the pixel cell size of the processed RADARSAT-1 F3 images, as well as with the spatial scale of our PSI analysis. The number of DS within the buffer zone is higher than that of DS intersecting the linear features, thereby resulting in an overall PS/DS ratio within the buffer zone only of ~0.6. Some of these MPs are certainly identified onto urban fabric and unrelated objects (e.g., houses, dwellings, light poles) surrounding the linear features of interest (see, for instance, Fig. 6h). Notwithstanding, we cannot neglect the presence of many MPs in the proximity of the aqueduct structures, especially over those southern sectors which are located over bare soil and agricultural fields. The predominance of DS against the PS within the buffer zone suggests that the surrounding land surface and road pavement have generated enough backscattering signal that can inform about the stability of the ground.

Tables 2–4 report the MP statistics with regard to the following three parameters, respectively:

1. building type – we consider ten classes of buildings, including the types of 'arch ruin', 'isolated arches', 'continuous arches' and 'arcades' that account for the different condition and architectural continuity of the aqueduct structures. While one up to three subsequent arches are classified here as isolated arches, an aqueduct section of more than 3 arches is grouped in the category 'continuous arches'. When the succession of arches runs

Table 2
Statistics of the MPs identified over the linear features with regard to structure type.

Structure types	N° of features	Relative %	MPs	PS	DS	% MPs	% PS	% DS	PS/DS ratio
Arcades	44	31.65	309	201	108	85.12	85.53	84.38	1.86
Arch ruin	27	19.42	5	3	2	1.38	1.28	1.56	1.50
Cistern	2	1.44	2	2	0	0.55	0.85	0.00	N/A
Continuous arches	11	7.91	28	18	10	7.71	7.66	7.81	1.80
Fountain	2	1.44	0	0	0	0.00	0.00	0.00	N/A
Gate	3	2.16	3	3	0	0.83	1.28	0.00	N/A
Isolated arches	8	5.76	4	3	1	1.10	1.28	0.78	3.00
Scatter	36	25.90	5	2	3	1.38	0.85	2.34	0.67
Tower	2	1.44	2	1	1	0.55	0.43	0.78	1.00
Wall	4	2.88	5	2	3	1.38	0.85	2.34	0.67

Table 3
Statistics of the MPs identified over the linear features with regard to structure planimetric orientation.

Structure orientation	N° of features	Relative %	MPs	PS	DS	% MPs	% PS	% DS	PS/DS ratio
E–W	10	11.11	18	10	8	5.25	4.52	6.56	1.3
N–S	11	12.22	76	73	3	22.16	33.03	2.46	24.3
NW–SE	59	65.56	243	134	109	70.85	60.63	89.34	1.2
SW–NE	10	11.11	6	4	2	1.75	1.81	1.64	2.0

over tens to hundreds of metres (up to kilometre length) without any interruption, that is classified as a proper 'arcade';
2. structure planimetric orientation – defined with regard to the north;
3. vegetation coverage – four classes from 'absent' to 'dominant' are considered to account for the vegetation grown over the buildings. Classification was done by using the 2008 orthophoto and 2009–2010 Google Earth imagery to match as much as possible the last acquisition date of the SAR data stack.

With regard to the first parameter, most of the aqueducts still consist of monumental arcades (Fig. 6a and b) and, secondarily, of continuous arches (Fig. 6c), with various degree of vegetation coverage (Fig. 6d; cf. Table 4). Clusters of isolated arches and arch ruins (Fig. 6e) are also located in the southern rural part of the ROI (i.e. the so-called Park of Aqueducts, parallel to Via Appio Claudio up to Via delle Capannelle; see Fig. 5). As expected, more than 85% of the MPs identified over the linear features in the ROI are spatially associable with the predominant building type of 'arcades' (Table 2), while 'continuous arches' are the second most covered building type (nearly 8% of the total MPs) with a similar PS/DS ratio (1.80 against 1.86). This analogous proportion between PS and DS finds explanation with the fact that the two building types are very similar and only differ in the architectural length.

Interestingly, similar values of MP densities are found over the 'arch ruin' and 'isolated arches' types. Over both these classes a few MPs were identified (slightly more than 2%), although these structures account for more than 20% of the total linear features within the ROI. An a priori assessment might have considered the morphology and nature of these man-made elements sticking out of the ground as beneficial factors to create backscattering conditions. Combinations of reduced size (5–70 m^2), orientation and vegetation coverage likely did not favour the MP identification at some extent, also in light of the 8 m-resolution of the SAR images processed.

Not surprisingly, the 'fountain', 'cistern', 'tower' and 'gate' types show the lowest MP densities, with values less than 1% of the total MP dataset, and no MPs identified over the fountains (Table 2). Nevertheless, these values need to be assessed in the context. Of the 3 gates included within the ROI, one coincides with the monumental entrance of Porta Maggiore (Fig. 6g). Taking into account the 10 m-buffer zone (and therefore the possible areas of radar backscattering at the bottom and in the surroundings of the monumental gate), 10 MPs can be spatially attributed to Porta Maggiore (i.e. equal to ~2.8% of the total MP dataset; cf. Fig. 9b), with a PS/DS ratio of 1.50. Therefore, despite the apparently limited number of MPs, the processing output was satisfactory.

Furthermore, in applications at the scale of single building, even one MP can be crucial to assess the condition, as highlighted in recent studies over urban and rural settlements (e.g., Tapete & Cigna, 2012b; Cigna et al., 2012a). This is also the case of the two MPs identified over the 'tower' type. As discussed in detail in Section 'Condition and damage assessment at large scale', although the two MPs found over the medieval tower Torre del Fiscale (cf. Fig. 12a) account for less than 1% of the total PSI dataset (Table 2), the deformation and height information they provide are proved essential to underpin the condition assessment of this building.

Low MP density values also depend on the structure orientation in respect of the ascending geometry of the right-looking RADARSAT-1 satellite, with consequent good or bad visibility of the object on the ground. As per Table 3, ~65.6% of the monitored structures are NW–SE oriented and are covered by the highest portion of the MPs (243, i.e. 70.85% of the total). This confirms that PSI processing output covers more than half of the building environment. PSI coverage increases up to ~93% if we also sum the 76 MPs identified over the N–S oriented sectors, which are the second most covered

Table 4
Statistics of the MPs identified over the linear features with regard to vegetation coverage.

Vegetation coverage	N° of features	Relative %	MPs	PS	DS	% MPs	% PS	% DS	PS/DS ratio
Absent	59	43.38	103	74	29	29.77	33.33	23.39	2.6
Few	48	35.29	194	117	77	56.07	52.70	62.10	1.5
Abundant	20	14.71	39	25	14	11.27	11.26	11.29	1.8
Dominant	9	6.62	10	6	4	2.89	2.70	3.23	1.5

orientation class across the ROI. With N–S orientation the number of the identified PS equals more than 24 times the number of DS. Considering that most of the N–S oriented structures are arcades and run over both the northern urban and southern rural areas of the ROI, such predominance of PS suggests that the geometry of the buildings allowed persistent conditions of strong radar backscattering throughout the RADARSAT-1 time series. The backscattering mechanisms mainly occurred at the corners formed by the bottom of the arcades with the surrounding soil or road pavement, since the vast majority of these MPs are spatially located at low heights compared with the ground elevation (cf. sample areas 5–7 in Fig. 7a).

As expected, low to very low numbers of MPs were retrieved over the E–W and SW–NE oriented buildings (Table 3), with PS/DS ratios still suggesting that more PS were found than DS. This further confirms the well known issue of limited MP identification over E–W oriented objects, and such evidence is achieved over structures belonging to building types (e.g., arcades and continuous arches) that generally provide satisfactory MP densities (cf. above). Therefore, we can conclude that in this case the orientation is the main limiting factor.

Vegetation coverage is another factor inhibiting the MP identification. The number of MPs over the linear features significantly decreases up to one order of magnitude from the 'absent' to 'dominant' classes, with the only exception of the 'few' class (Table 4). The latter shows the highest MP percentage (i.e. ~56% of the total), which is explained by the fact that, over those sectors of the aqueducts, the vegetation is very concentrated and can only create local interference. Regardless the vegetation coverage degree, PS are always more abundant than DS.

$h_{MP} - h_{GPS}$ correlation

Fig. 5 reports the location of the sample areas, hereinafter called as follows (from south to north):

1) Aqua Claudia – Capannelle;
2) Aqua Claudia – Appio Claudio;
3) Aqua Claudia – railway;
4) Torre del Fiscale;
5) Felice Aqueduct – Vicolo dell'Acquedotto Felice;
6) Felice Aqueduct – Via Frascati;
7) Porta Maggiore.

The above were selected across the whole ROI based on the preliminary assessment, to be statistically representative of the different types of man-made structures (cf. classification in Section 'Numerical analysis of MP distribution vs. object properties' and Table 2), as well as of the deformation patterns observed. RTK GPS and DISTO height measurements have been collected following the procedure described in Section 'Topographic surveying'.

The scatter plot in Fig. 7a shows the correlation between h_{GPS} and h_{MP}, with the related standard deviation. It is apparent that, compared with the ground level, the identified MPs can be basically divided into two main classes: (i) those which are localized at the ground level up to the lower elevation of the man-made structures, and (ii) those which take h_{MP} values along the middle to the upper elevation of the surveyed objects. In particular the former are much more abundant of the latter, meaning that the barycentre of most of the MPs is located at low heights compared with the building elevation. Therefore we can infer that the corners formed by the ground and the base of the buildings were the most likely dihedral geometry to create conditions for radar backscattering mechanisms, especially in the middle to northern sectors of the analysed ROI (i.e. areas 3–7).

Such distribution of the whole PSI dataset is also confirmed by the associated histogram in Fig. 7b, which reports the classes of the identified MPs characterized by a certain value of Δh, i.e. h_{MP} minus h_{GPS}, the latter being the RTK GPS measurement of the ground elevation. 68.3% of the sample h_{MP} values spatially fall within the height interval from the ground level to +2 m, whereas only 19.6% are spatially attributed to the upper part of the buildings. Accounting for the respective SD_{hMP}, those MPs which fall within the negative Δh class −2 to 0 m have been geolocated below the ground level at which the RTK GPS measurement was taken, i.e. in ground depressions. The only sample h_{MP} value with $\Delta h < -2$ m coincides with a DS point (see red circle (in the web version) in the scatter plot in Fig. 7a) that is located in the valley close to the sample sector 3 (Aqua Claudia – railway). h_{GPS} and h_{MP} correlation thereby confirmed the GIS-based spatial interpretation.

The scatter plot also allows us to differentiate among the sample sectors (Fig. 7a). While all the MPs identified over the Aqua Claudia – Capannelle (area 1) are located along the elevation of the arcades, bimodal distribution is observed over the Aqua Claudia – Appio Claudio (area 2). 52.9% of the MPs are located in the middle to the upper part of the monumental arcades, with h_{MP} values from ~114 m to a maximum of 123 m, respectively. The latter value physically coincides with the so-called *specus*, i.e. the concrete water channel running atop the arcades which is, in most of the cases, partially preserved (cf. Fig. 6c and d).

The first example discussed in Section 'Condition and damage assessment at large scale' well demonstrates the value that the height information can add to the MP spatial interpretation, to the scope of monitoring the condition of buildings with high elevation, surrounded by ground with regular or irregular topography.

RTK GPS and DISTO validation

Results of the validation of the h_{MP} values and 3D geolocation of the MPs across the ROI are shown in Fig. 8, where the reliability of the methodology proposed in Section 'Methodology' was assessed by cross-comparing:

(i) h_{MP}–h_{GPS} pairs, without distinguishing between PS and DS (Fig. 8a);
(ii) h_{DS}–h_{GPS} pairs (Fig. 8b);
(iii) h_{PS}–h_{GPS} pairs (Fig. 8c);
(iv) h_{MP}–h_{est} pairs (Fig. 8d).

The top-left scatter plot in Fig. 8a summarizes the validation of the MP height information via the sample surveying campaign by RTK GPS, and confirms that the procedure of spatial attribution of the identified MPs to the objects on the ground as per Sections 'GIS-based data integration and preliminary assessment' and 'Topographic surveying' is correct and reliable (R^2 equals 0.970, and the slope of the linear regression equals 0.97). We also need to consider that the scatter plot in Fig. 8a compares both h_{DS}–h_{GPS} and h_{PS}–h_{GPS} pairs altogether, as a unique dataset. But, of course, these pairs rely on the different spatial meaning of DS with regard to PS, and their associated spatial uncertainties. To account for the above and assess separately the performance of the methodology proposed with regard to these two main groups of MPs, Fig. 8b and c show the validation results by splitting the sample h_{DS} from h_{PS} values. Interestingly, both the scatter plots highlight very satisfactory correlation, with R^2 of 0.974 and 0.970, and slopes of the linear regression equal to 0.95 and 0.99, respectively, thereby suggesting that the GNSS-based methodology applies successfully on both PS and DS.

The differences observed between the radar target elevations and h_{GPS} values relate, in part, to the assumption that we made

during the GIS-based preliminary assessment, i.e. that each MP falls over the object with which it visually overlaps according to the GIS multi-layering. Nonetheless, the constant shift observed between the h_{MP}, h_{PS} and h_{DS} and the corresponding h_{GPS} values (cf. values of the intercept of the linear regressions in Fig. 8a–c) seems to suggest the presence of an absolute elevation error in the SqueeSAR™ data. This error could have been brought in by the input DEM which was used during the PSI processing to model the initial topographic phase components (i.e. the SRTM in the analysed dataset), with respect to more accurate elevation values provided by the GPS (see, for instance, Gorokhovich & Voustianiouk, 2006). Due to the different nature of the MPs, the h_{DS}-h_{GPS} linear equation shows greater intercept (i.e. ~5.6 m), with respect to that of the h_{PS}-h_{GPS} linear equation, for which ~1.4 m intercept is observed. On the other hand, the correlation coefficients and values of the slope of the linear regressions that we obtained and almost equal to 1 reveal that the assumption made on the location of the MPs and the surveyed elevation by using the GPS (cf. Section 'Methodology') was valid, despite its intrinsic subjectivity.

Correlation still keeps high even when we cross-compare h_{MP} and h_{est} values (Fig. 8d; R^2 equals 0.953), with an intercept of the linear equation on the order of a few decimetres. Despite the coarseness of the ancillary surveying method by DISTO with respect to the RTK GPS, the validation results suggest that h_{est} values can be reliably used when other topographic/architectural measurements are unfeasible. In this regard, the recommendations reported in Section 'Complementary laser distance meter survey' to increase the precision and, therefore, the repeatability of the DISTO measurements aim to prevent the addition of further errors.

Mapping patterns at small scale

The practical advantage of the h_{MP}–h_{GPS} cross-referencing discussed in the previous sections lies on the fact that we now have the environmental knowledge to reclassify the MPs of the entire PSI dataset based on their h_{MP} values against the local ground level and structure geometry. This allows the operator to generate a map where the MPs are immediately discriminated based on their height spatial location, i.e. by converting the type of information that was previously displayed in the scatterplot of Fig. 7a into an easy-to-use visual product.

Fig. 9a and b reports two zooms of the reclassification map over the survey areas 1 and 7, i.e. Aqua Claudia – Capannelle and Porta Maggiore, respectively, with three main classes of spatial location: at ground level, along the elevation of the structure and atop the structure. The selected survey areas here selected are demonstrative examples of two opposite situations: most of the barycentres of the detected deformation are located at the top of the structures, so that we can infer that the conservation issue relates with the stability of the buildings themselves (Fig. 9a); or mainly at the bottom of the structures or along the first meters of the structure elevation, meaning that causes for motions can include instability at the ground level (Fig. 9b).

The main implication of this type of reclassification is that we can discriminate condition of the building sectors at small scale across the ROI, and fuse the height information with the deformation estimate to zone the patterns of concern against those that are negligible. Fig. 9c and d show the result of the data fusion for the sample areas 1 and 7. Colour scale (in the web version) and renderers used here reflect the LOS velocity values of the MPs and the outcome of the spatial localization of MPs, respectively. Deformation patterns are classified according to the definitions reported in Section 'Deformation analysis and condition assessment' of the proposed methodology.

This map serves as final product to guide the geographer in designing the large-scale investigations to undertake in those sectors that are found critical or ambiguous. For instance, in the sample area of Via delle Capannelle (Fig. 9a and c), the synoptic view reveals that only one transect of the arcades requires priority attention, since it is probable that deformation affected the top of the structure during the monitoring period (cf. Fig. 13 for the benefits obtained in this case). Conversely, in the sample area of Porta Maggiore (Fig. 9b and d), more sectors show deformation in the period 2003–2010, but with a different spatial location of the MPs. Thinking in the perspective of geographical implementation, this means that a different approach of site investigation needs to be implemented (e.g., detailed inspection of the lower brick-wall masonry close to the ground level), even for neighbouring structures (cf. the two yellow polygons (in the web version) in the NE corner of Porta Maggiore).

Condition and damage assessment at large scale

Three examples are discussed here to demonstrate how the height information of PS and DS can be beneficially exploited to address the deformation analysis at large scale, with particular regard to the following common situations:

a. spatial distribution of the h_{MP} values across the elevation of the building suggests that deformation have affected different architectural portions of the structure and/or occurred at the ground level;
b. 'alarming' deformation pattern is identified over a building or a cluster of structures but, dependently on the building type, the height information can contribute to understand the mechanism and impact of the observed deterioration processes;
c. 'ambiguous' sector where, despite the relatively stable V_{LOS} value, trend inversion or changes are detected within the time series and could relate with ongoing deterioration processes or existing damages, the location of which could be confirmed by h_{MP}.

Fig. 10 shows the MP spatial distribution retrieved over the sample area 2 (i.e. Aqua Claudia – Appio Claudio; cf. Fig. 5 for location in the ROI). Based on the preliminary assessment, this sector was classified as 'alarming', especially if compared with the MP density of the subsequent section of the aqueduct (Fig. 10a). The latter indeed appeared relatively stable from the MP time series, and ground truth campaign did not highlighted any surface damage or warning element (Fig. 10d). These SAR-based evidences were particularly significant since they justified the targeted interventions carried out by the local conservators over the sample area 2 in the years after the last RADARSAT-1 acquisition. By exploiting the RTK GPS-aided 3D geolocation and validation of the h_{MP}, part of the detected deformation (with average V_{LOS} of −2.0 mm/yr over the whole period March 2003–February 2010) were attributed to motions at the bottom of the arcades. Conversely, other MPs with average V_{LOS} of −2.2 mm/yr were correlated with the instability of the stone blocks of the arches (Fig. 10b) and the outer brick curtains detaching from the concrete core of the *specus* (Fig. 10c). The fact that deformation have been localized at low elevations was assumed as a warning indicator of potential ground instability. Recommendations were therefore made to undertake further checks with targeted ground investigations.

Similar conservation strategy was suggested for the northern section of the arcades (top-left corner in Fig. 10a), where the deformation pattern was defined by downward moving DS located at low elevation compared with the ground level, against relatively

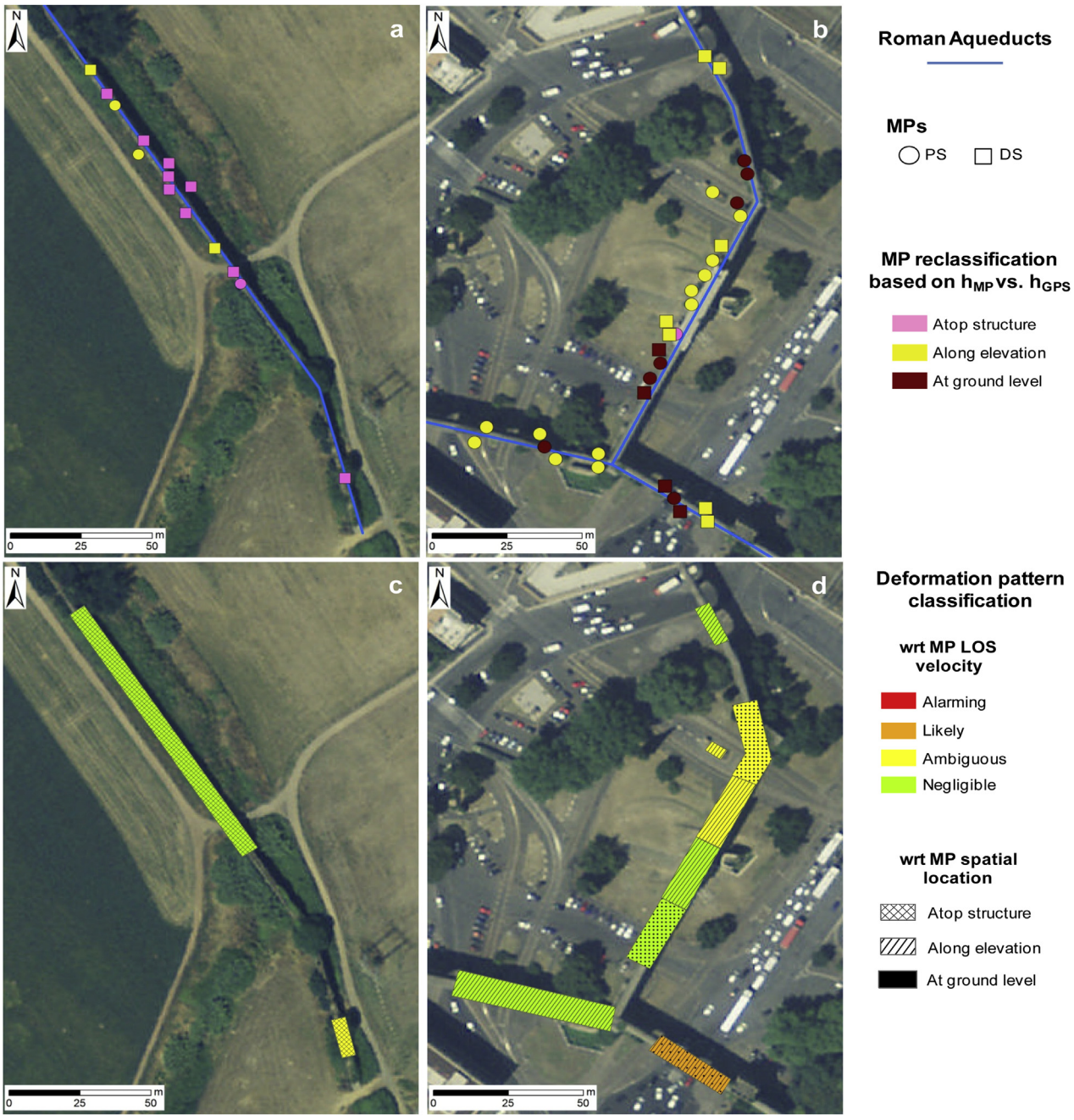

Fig. 9. Reclassification of the MPs detected over the sample areas (a) 1 – Aqua Claudia – Capannelle and (b) 7 – Porta Maggiore, based on h_{MP} – h_{GPS} cross-referencing (cf. Fig. 7). c and d) Final mapping with deformation pattern classification fusing the velocity and height spatial information.

stable PS and DS located at the top of the structures (see interpretational section A–A′ in Fig. 11).

Very alarming deformation pattern was detected over the medieval tower in sector 4 (i.e. Torre del Fiscale; cf. Fig. 5 for location in the ROI). Guided by the deformation pattern classification map (see inset in Fig. 12a), the assessment was done based on the following MPs and related parameters (anticlockwise from NW corner of the tower to the neighbouring arcade of the Felice Aqueduct in SE; Fig. 12a): *PS A7JIV*, V_{LOS} −4.94 ± 0.75 mm/yr, h_{MP} 102.4 ± 1.92 m; *DS A7JIO*, V_{LOS} −5.01 ± 0.75 mm/yr, h_{MP} 104.05 ± 1.83 m, Effective Area (EA) 483 m^2; *PS A7JII*, V_{LOS} −5.05 ± 0.8 mm/yr, h_{MP} 103.37 ± 2.02 m. The consistency in terms of average LOS motion rate (i.e. ~5.0 mm/yr), displacement trend of the associated time series and height values suggests that the above MPs depict the same deterioration process that affects locally the tower. The comparison with the relative stability observed over the surrounding suburban context enhances the tower deformation, as clearly shown by the results of the Kriging interpolation reported in Fig. 12b.

Based on RTK GPS validation, deformation estimates were spatially attributed to the lower portion of the monument. The base structure supporting the rest of the tower elevation coincides with the mixed masonry formed by the remnants of the stone arches of the former Roman Aqueducts that intermingle with the medieval brickwork (Fig. 12c). The cracks along the old brickwork repairs and patches (see red dashed lines as pictured in Fig. 12d prior to the recent restoration) were further surface indicators warning about

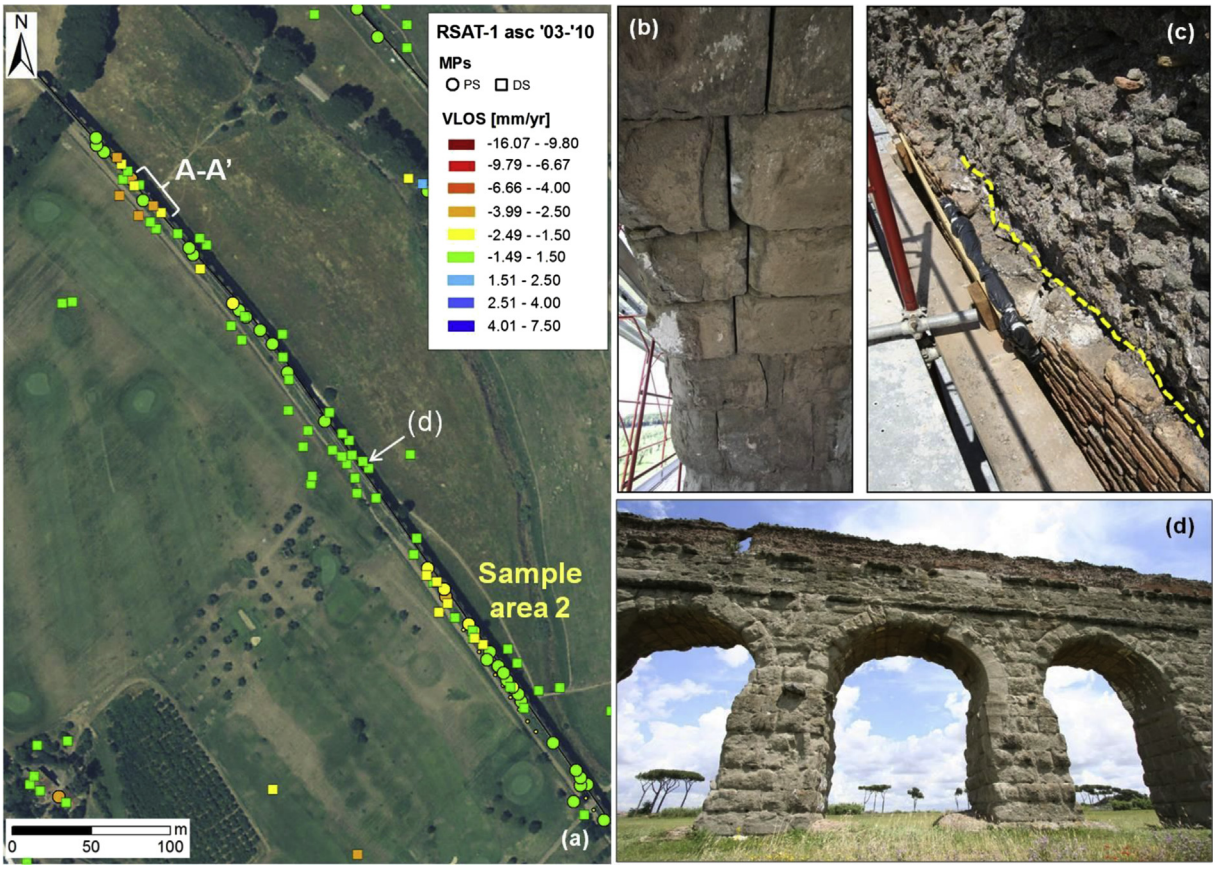

Fig. 10. a) Spatial distribution of RADARSAT-1 F3 ascending MPs (2003–2010) over the sample area 2 (Aqua Claudia – Appio Claudio; see location in Fig. 5) and the subsequent sectors of the Claudian Aqueduct arcades (cf. Fig. 6a), with indication of section A–A′ showed in Fig. 11. b) Details of cracks in the arch intrados and c) detachment of the brick curtains from the concrete core of the *specus*, observed in the arcades of the sample area 2. d) View of the arcades from the middle sector (see white arrow in picture a), for which MPs show stability.

the effects of the instability of the tower. These evidences also suggested that causes of instability should be searched in ground instability, as well. As inferred by the local geological setting (cf. Fig. 5), cavities and subterranean tunnels within the tuff run underneath the land in the proximity of the tower, and collapses events are recorded in the history of this area.

It is worth noting here that the absence of MPs at higher elevation (i.e. at the top of the tower) does not allow us to exclude that faster deformation have occurred at an extent that could have compromised the PSI processing (although the limit of 20 cm/yr for C-band RADARSAT constellation satellites – cf. in this regard Cigna, Bianchini, & Casagli, 2013 – seems unlikely to have been passed).

Time series analysis managed with (semi-)automated methods of PSI classification can help to prevent erroneous interpretation of MPs due to misleading V_{LOS} value falling within the stability threshold (e.g. within the interval of ±1.5 mm/yr in this case).

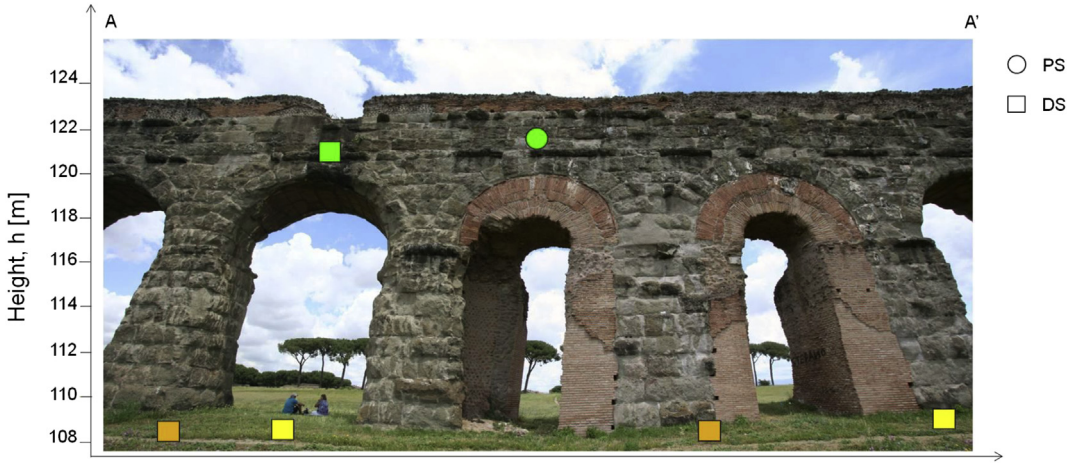

Fig. 11. Spatial interpretation of the MPs along the elevation of section A–A′ of the Claudian Aqueduct arcades (see location and MP colour coding in Fig. 10a), based on the RTK GPS and DISTO validation of the h_{MP} values. (For interpretation of the references to colour in this figure legend, the reader is referred to the web version of this article.)

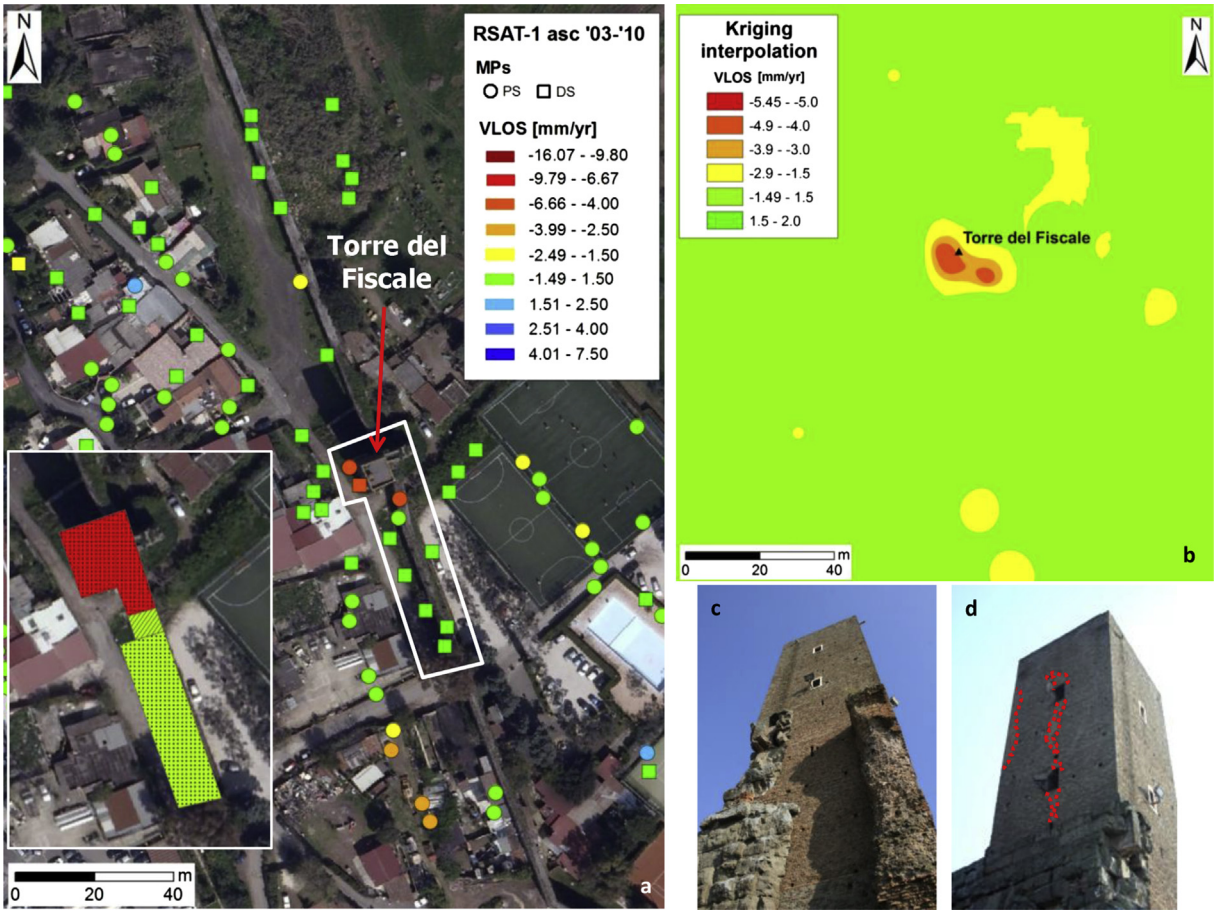

Fig. 12. a) Spatial distribution of RADARSAT-1 F3 ascending MPs (2003–2010) over the sample area 4 – Torre del Fiscale (see location in Fig. 5) that was classified as 'alarming' as shown in the inset reporting the deformation pattern classification map (cf. Fig. 9c and d for the legend). b) Kriging interpolation results enhance the deformation pattern over the medieval tower with LOS displacements away from the satellite. Views of c) the western and d) northern façades of the tower as appeared in 2010 before the recent restoration. Red dotted lines in d) highlight the repairs and cracks visible at that time. (For interpretation of the references to colour in this figure legend, the reader is referred to the web version of this article.)

Following the procedure of Deviation Index 1 (DI_1) calculation described in Cigna, Tapete, and Casagli (2012b) and then applied to archaeological heritage by Tapete and Casagli (2013), trend changes were detected within the time series of DS A5JFO in sector 1 (i.e. Aqua Claudia – Capannelle; Fig. 13a–c; cf. Fig. 5 for location in the ROI). As discussed in the previous section, the final mapping product with deformation pattern classification reports an 'ambiguous' polygon over the last arcades in the southern end of this sector (Fig. 9c). Despite the V_{LOS} of +0.07 mm/yr, inversions of displacement trends are recorded throughout the period 2003–2010 (Fig. 13b). DI_1 computation across the time series highlighted that the major trend deviation was observed as of the 24/08/2005 SAR acquisition (Fig. 13c), with a DI_1 of 3.89 as the highest value observed throughout the time series (except for a previous peak mostly due to occasional high discrepancy between consecutive LOS estimates). August 2005 can be therefore assumed as the major t_{break} for this DS, which at the end cannot be considered 'stable'. In light of the spatial uncertainty due to the DS nature, we cross-compared the h_{MP} 122.58 ± 1.38 m with the local ground and atop-structure h_{GPS} values, the latter being 122.68 m. This comparison was crucial to spatially refer the deformation estimate to the existing damages of the structure. The arcade, built of tuff blocks and partially covered by wild vegetation at the time of the monitoring (Fig. 13d), already showed deterioration of the exposed surfaces (Fig. 13e). At the location of the DS A5JFO huge cracks were found running across the extrados of the arch (Fig. 13f), as a clear indicator of ongoing structural instability and progressive opening of the stonework.

Conclusions

In this paper we propose a desk-based and in-situ surveying method to exploit the spatial information provided by point-wise measurement points (MPs) obtained from multi-temporal Persistent Scatterer Interferometry (PSI) processing of synthetic aperture radar (SAR) imagery, that are increasingly used in the field of geospatial analysis of deformation due to ground and structure instability. To investigate how to best implement this technique in geographical applications aimed to discriminate differential condition of buildings and zone the areas where to undertake ground investigations and inspections, we addressed the following two aspects: (i) solving the spatial uncertainty that is commonly faced when working with highly dense outputs from PSI processing providing not only persistent but also distributed scatterers, i.e. MPs the deformation estimate of which refers to either point-wise targets or an area; and (ii) demonstrating how height information (h_{MP}) can be converted and fused into a map product to understand (or at least infer) where the detected deformation and presumably their causes are located.

We therefore developed an accurate and repeatable method to retrieve micro-topographic measurements by RTK GPS (and complementary survey by DISTO device), which offers a good

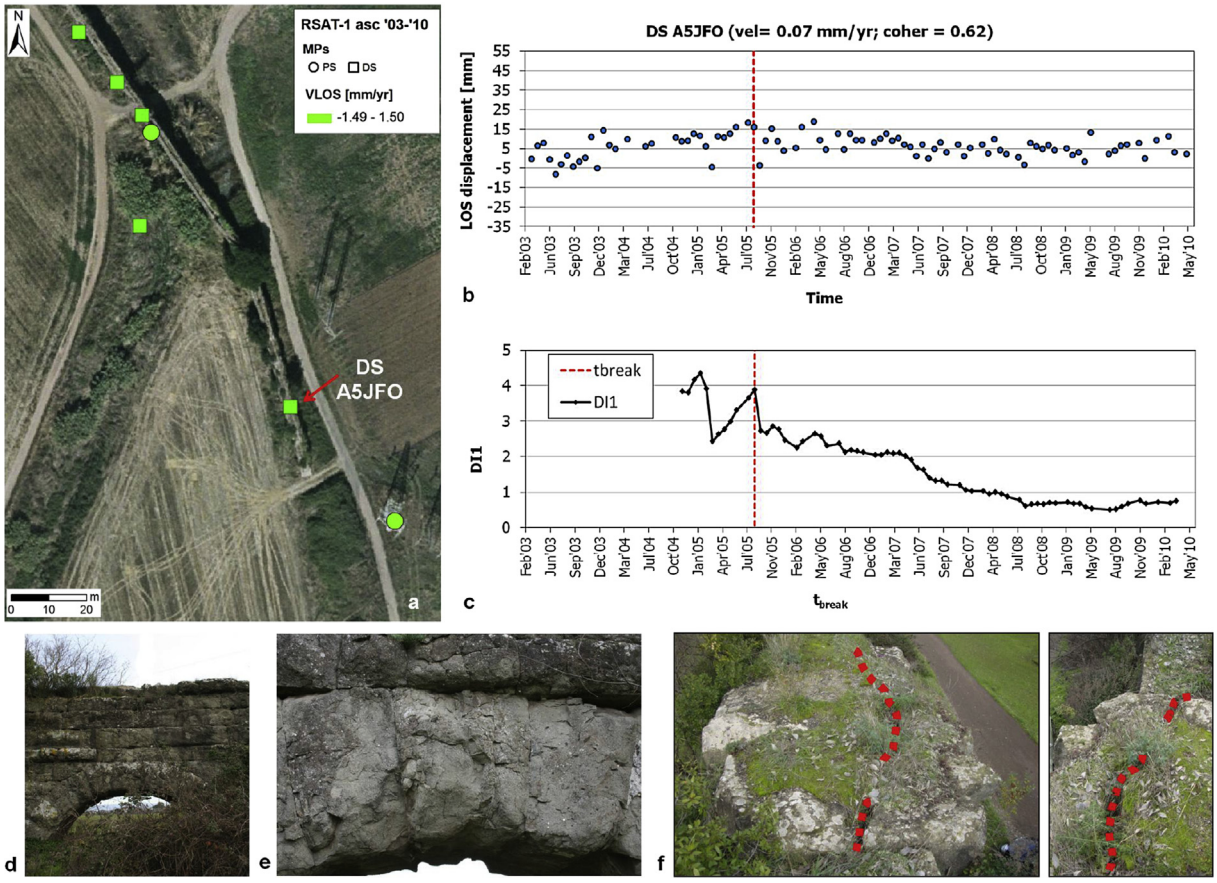

Fig. 13. a) Spatial distribution of RADARSAT-1 F3 ascending MPs (2003–2010) over the sample area 1 (Aqua Claudia – Capannelle; see location in Fig. 5 and cf. pattern classification in Fig. 9a and c). b) Time series of DS A5JFO (cf. picture a for its position) and c) graph of DI_1 vs. t_{break} computed via the method by Cigna et al. (2012b) and Tapete and Casagli (2013). Detailed views of: d) the arcade which the DS refers to, e) surface deterioration of the tuff blocks, and f) cracks running over the arch extrados (red dotted lines). (For interpretation of the references to colour in this figure legend, the reader is referred to the web version of this article.)

compromise between reliability, easy implementation in the field, reduced costs and limited time-consumption, for those geographers and remote sensing experts, as well as for practitioners and urban managers who use PSI data but do not necessarily have costly facilities and funds to monitor and assess condition of huge building environments.

We purposely tested this methodological procedure over kilometre-wide peri-urban to rural ROI in southern Rome, Italy, focusing the attention on linear features and structures belonging to the local historical assets.

Critical discussion of the MP densities with regard to the properties of the surveyed objects highlighted interesting relationships, and enhanced the different spatial nature of DS with respect to PS targets.

Numerical analysis of sample h_{MP}–h_{GPS} pairs resulted in high correlation, and confirmed that across the ROI two main classes of h_{MP} can be distinguished with regard to the ground level and the top elevation(s) of the structure. Cross-comparison via scatter plots proved that RTK GPS and integration with DISTO measurements can be a valid alternative for in-situ validation of MP 3D geolocation, against the idea that this combination could be less suitable than more accurate surveying methods such as LiDAR, high resolution DEMs/DSMs or products from UAV and structure-from-motion.

Of course, sampling is crucial to obtain a reliable and comprehensive representation of the whole ROI, and preliminary assessment and MP statistics are certainly key steps of the procedure to select the sample areas. On the other side, in-situ validation is an unavoidable requirement as the complexity of the building environment increases.

From a point of view of practical implementation in real-world applications, the cross-referencing of h_{MP} and h_{GPS} serves here not only to prove numerically the accuracy and validity of the method, but also to illustrate how a geographer should select sample areas, collect micro-topographic survey data and use the height and elevation values from RTK GPS and DISTO to reclassify the available MPs. The outcomes of the MP reclassification feeds into the final mapping product that allows discrimination of the differential condition between building sectors and within each sector, at small to large scales, and prepares for the design of local investigation and inspection activities.

In this regard, the examples discussed in this paper clearly show the improvement achieved in the radar interpretation by resolving spatial uncertainty of PSI datasets. Deformation of constructions such as towers and tall buildings (in this case, arcades and arches) cannot be analysed only based on the planimetric position inferred from the GIS multi-layering, but are also to be assessed and interpreted along the elevation above the local ground level. In most of the cases analysed in Rome, Italy, observed deformation were attributed to motions at the bottom of the structures, with the consequence of addressing further investigations to assess potential hazards from ground instability. In other situations, the MP spatial location along the building elevation matches with in-situ evidence of instability and damages of single architectural components.

Looking at the most recent innovation in radar space science, the outcomes obtained from the implementation on PSI data from 8-m resolution RADARSAT-1 imagery suggest that this approach can be replicated with products from high resolution SAR imagery (e.g., X-band TerraSAR-X and COSMO-SkyMed, and the C-band Sentinel-1A), which are expected to provide much more abundant MP densities, with higher ratio of MPs per single building. Therefore, we believe that the MP height information deserves more attention that done so far in SAR-based applications. The impact of a research like ours aimed to develop ways to 3D-geolocate surface scatterers obtained from PSI also lies on the fact that distributed scatterers are nowadays sought to increase the MP density. With no doubt, understanding the spatial meaning of the deformation estimates helps to tailor the restoration and maintenance activities on historical buildings, thereby preventing the execution of useless costly interventions, and instead optimizing the available resources.

This, of course, is highly relevant in a field of geographic application where optimization of resources is crucial. With an end-user's perspective, our research aims to favour a more aware use of this emerging technology, and contributes to fill a gap in the existing applied geographic literature with specific regard to the spatial dimension involved in the use of InSAR for building surveying.

Acknowledgements

This research was carried out in the framework of the project "Monitoraggio radar satellitare dell'area archeologica di Roma e integrazione delle risultanze del monitoraggio GB-InSAR del Colle Palatino (gennaio-marzo 2010)" funded by the Italian Ministry of Cultural Heritage and Activities and Tourism (MiBACT), and was part of the PhD and postdoctoral research of D. Tapete. The authors gratefully acknowledge R. Cecchi, formerly Commissioner for the Archaeological Heritage of Rome and Ancient Ostia on behalf of MiBACT, and P. Petrangeli from the Archaeological Superintendence of Rome for their support. The authors also thank the archaeologists and architects of the State and Municipal Archaeological Superintendences of Rome for their co-operation, and provision of historical and conservation background inputs. SqueeSAR™ processing of RADARSAT-1 data was performed by TeleRilevamento Europa s.r.l. (TRE). Methodology design, radar interpretation and geospatial analysis were carried out by D. Tapete, while the RTK GPS survey campaign was led by S. Morelli. 2008 orthophoto was accessed via the WMS service of the National Geoportal of the Italian Ministry of Environment, Territory and Sea.

References

Ali, Z., Tuladhar, A., & Zevenbergen, J. (2012). An integrated approach for updating cadastral maps in Pakistan using satellite remote sensing data. *International Journal of Applied Earth Observation and Geoinformation, 18*, 386–398.

Barkovic, D., Zrinjski, M., & Boric, B. (2013). Laboratory procedure for the calibration of laser hand-held distance meter. In *13th SGEM GeoConference on Informatics, Geoinformatics And Remote Sensing, SGEM2013 Conference Proceedings, June 16-22, 2013* (Vol. 2, pp. 293–300). http://dx.doi.org/10.5593/SGEM2013/BB2.V2/S09.038.

Bateson, L., Cuevas, M., Crosetto, M., Cigna, F., Schijf, M., & Evans, H. (2012). *PANGEO: Enabling access to geological information in support of GMES: Deliverable 3.5 production manual. Version 1.3*. Available at http://www.pangeoproject.eu/sites/default/files/pangeo_other/D3.5-PanGeo-Production-Manual-v1.3.pdf. Last accessed 28.05.14.

Bhaskaran, S., Paramananda, S., & Ramnarayan, M. (2010). Per-pixel and object-oriented classification methods for mapping urban features using Ikonos satellite data. *Applied Geography, 30*(4), 650–665. ISSN 0143-6228.

Bianchini, S., Tapete, D., Ciampalini, A., Di Traglia, F., Del Ventisette, C., Moretti, S., et al. (2014). Multi-temporal evaluation of landslide-induced movements and damage assessment in San Fratello (Italy) by means of C- and X-band PSI data. In E. Pardo-Igúzquiza, C. Guardiola-Albert, J. Heredia, L. Moreno-Merino, J. J. Durán, & J. A. Vargas-Guzmán (Eds.), *Mathematics of planet earth. Lecture notes in earth system sciences* (pp. 257–261). Berlin Heidelberg: Springer-Verlag.

Bock, Y., Wdowinski, S., Ferretti, A., Novali, F., & Fumagalli, A. (2012). Recent subsidence of the Venice Lagoon from continuous GPS and interferometric synthetic aperture radar. *Geochemistry, Geophysics, Geosystems Research Letter, 13*(3). http://dx.doi.org/10.1029/2011GC003976.

Cecchi, R., & Gasparoli, R. (2010). *Prevenzione e manutenzione per i Beni Culturali edificati. Procedimenti scientifici per lo sviluppo delle attività ispettive*. Il caso studio delle aree archeologiche di Roma e Ostia Antica. Firenze: Alinea Editrice, 345 pp.

Cecchi, R., & Gasparoli, R. (2011). *La manutenzione programmata dei Beni Culturali edificati. Procedimenti scientifici per lo sviluppo di piani e programmi di manutenzione*. Casi studio su architetture di interesse archeologico a Roma e Pompei. Firenze: Alinea Editrice, 381 pp.

Chang, L., & Hanssen, R. F. (2014). Detection of cavity migration and sinkhole risk using radar interferometric time series. *Remote Sensing of Environment, 147*, 56–64. http://dx.doi.org/10.1016/j.rse.2014.03.002.

Cigna, F., Bianchini, S., & Casagli, N. (2013). How to assess landslide activity and intensity with Persistent Scatterer Interferometry (PSI): the PSI-based matrix approach. *Landslides, 10*, 267–283. http://dx.doi.org/10.1007/s10346-012-0335-7.

Cigna, F., Del Ventisette, C., Gigli, G., Menna, F., Agili, F., Liguori, V., et al. (2012a). Ground instability in the old town of Agrigento (Italy) depicted by on-site investigations and Persistent Scatterers data. *Natural Hazards and Earth System Sciences, 12*, 3589–3603. http://dx.doi.org/10.5194/nhess-12-3589-2012.

Cigna, F., Lasaponara, R., Masini, N., Milillo, P., & Tapete, D. (2014). Persistent Scatterer Interferometry Processing of COSMO-SkyMed StripMap HIMAGE Time Series to Depict Deformation of the Historic Centre of Rome, Italy. *Remote Sensing, 6*, 12593–12618. http://dx.doi.org/10.3390/rs61212593.

Cigna, F., Tapete, D., & Casagli, N. (2012b). Semi-automated extraction of Deviation Indexes (DI) from satellite Persistent Scatterers time series: tests on sedimentary volcanism and tectonically-induced motions. *Nonlinear Processes in Geophysics, 19*, 643–655. http://dx.doi.org/10.5194/npg-19-643-2012.

Comerci, V., Cipolloni, C., Di Manna, P., Guerrieri, L., Vittori, E., Bertoletti, E., et al. (2012). *Enabling access to geological information in support of GMES*. D7.1.26 Geohazard Description for Rome V 1.0, 15/12/2012, 175 pp. Available online http://www.pangeoproject.eu/. Last accessed 28.05.14.

Crosetto, M., Monserrat, O., Jungner, A., & Crippa, B. (2009). Persistent Scatterer Interferometry: potential and limits. In C. Heipke, K. Jacobsen, S. Müller, & U. Sörgel (Eds.), *ISPRS archives – Volume XXXVIII-1-4-7/W5, 2009, WG I/2, I/4, IV/2, IV/3, VII/2, ISPRS Hannover Workshop 2009, High-Resolution Earth Imaging for Geospatial Information, June 2-5, 2009, Hannover, Germany*.

Delgado Blasco, M., Hendrickx, M., De Laet, V., Verstraeten, G., & Hanssen, R. (Sept 2012). PS-InSAR and Change Detection techniques for analyzing the 3D evolution of Cairo and its surroundings from 2004 to 2010. In *3rd Workshop on Remote Sensing for Archaeology and Cultural Heritage Management, Ghent* (pp. 19–22).

Dong, Y., Li, Q., Dou, A., & Wang, X. (2011). Extracting damages caused by the 2008 Ms 8.0 Wenchuan earthquake from SAR remote sensing data. *Journal of Asian Earth Sciences, 40*(4), 907–914.

EC. (2011). *Urban Atlas*. it001l_roma. Available at http://www.eea.europa.eu/data-and-maps/data/urban-atlas/. Last accessed 02.07.14.

English Heritage. (2011). *National Heritage Protection Plan 2011-15*. Progress Report May-September 2011.

European Parliament. (2007). *Protecting the cultural heritage from natural disasters*. IP7B7CULT/IC/2006_163, 23/02/2007, 100 pp.

Featherstone, W. E., & Stewart, M. P. (2001). Combined analysis of real-time kinematic GPS equipment and its users for height determination. *Journal of Surveying Engineering, 127*(2), 31–51. http://dx.doi.org/10.1061/(ASCE)0733-9453(2001)127:2(31).

Ferretti, A., Fumagalli, A., Novali, F., Prati, C., Rocca, F., & Rucci, A. (2011). A new algorithm for processing interferometric data-stacks: SqueeSAR™. *IEEE Transactions on Geoscience and Remote Sensing, 49*(9), 3460–3470. http://dx.doi.org/10.1109/TGRS.2011.2124465.

Ferretti, A., Prati, C., & Rocca, F. (2001). Permanent scatterers in SAR interferometry. *IEEE Transactions on Geoscience and Remote Sensing, 39*, 8–20. http://dx.doi.org/10.1109/36.898661.

Frondoni, R., Mollo, B., & Capotorti, G. (2011). A landscape analysis of land cover change in the Municipality of Rome (Italy): spatio-temporal characteristics and ecological implications of land cover transitions from 1954 to 2001. *Landscape and Urban Planning, 100*(1–2), 117–128.

Giordano, G., De Benedetti, A. A., Diana, A., Diano, G., Gaudioso, F., Marasco, F., et al. (2006). The Colli Albani mafic caldera (Roma, Italy): stratigraphy, structure and petrology. *Journal of Volcanology and Geothermal Research, 155*(1–2), 49–80. http://dx.doi.org/10.1016/j.jvolgeores.2006.02.009.

Gorokhovich, Y., & Voustianiouk, A. (2006). Accuracy assessment of the processed SRTM-based elevation data by CGIAR using field data from USA and Thailand and its relation to the terrain characteristics. *Remote Sensing of Environment, 104*, 409–415. http://dx.doi.org/10.1016/j.rse.2006.05.012.

Hofmann-Wellenhof, B., Lichtenegger, H., & Collins, J. (2001). *GPS – Theory and practice* (7th ed.). Wien: Springer-Verlag.

Iadanza, C., Cacace, C., Del Conte, S., Spizzichino, D., Cespa, S., & Trigila, A. (2013). Cultural heritage, landslide risk and remote sensing in Italy. In C. Margottini, P. Canuti, & K. Sassa (Eds.), *Risk assessment, management and mitigation: Vol. 6. Landslide science and practice* (pp. 491–499). Berlin Heidelberg: Springer.

Jat, M. K., Garg, P. K., & Khare, D. (2008). Monitoring and modelling of urban sprawl using remote sensing and GIS techniques. *International Journal of Applied Earth Observation and Geoinformation, 10*(1), 26–43.

Karner, D. B., Marra, F., & Renne, P. R. (2001). The history of the Monti Sabatini and Alban Hills volcanoes: groundwork for assessing volcanic–tectonic hazards for Rome. *Journal of Volcanology and Geothermal Research, 107*, 185–219.

Kourkouli, P., Strozzi, T., & Wegmuller, U. (2012). Comparison of DInSAR and persistent scatterer interferometry for ground-motion monitoring in the Venice lagoon. In *Geoscience and Remote Sensing Symposium (IGARSS), 2012 IEEE International* (pp. 3919–3922). http://dx.doi.org/10.1109/IGARSS.2012.6350555.

Liu, T., & Yang, X. (2015). Monitoring land changes in an urban area using satellite imagery, GIS and landscape metrics. *Applied Geography, 56*, 42–54.

Mcnally, A. J. D., & Mckenzie, S. J. P. (2011). Combining multispectral aerial imagery and digital surface models to extract urban buildings. *Journal of Maps, 7*(1), 51–59.

Morelli, S., Battistini, A., Segoni, S., Manzo, G., Ermini, L., & Catani, F. (2014). A cost effective methodology for the rapid evaluation of the flood susceptibility along anthropized rivers. In G. Lollino, D. Giordan, C. Marunteanu, B. Christaras, I. Yoshinori, & C. Margottini (Eds.), *Engineering geology for society and territory* (Vol. 5). Switzerland: Springer International Publishing. http://dx.doi.org/10.1007/978-3-319-09048-1_164.

Morelli, S., Segoni, S., Manzo, G., Ermini, L., & Catani, F. (2012). Urban planning, flood risk and public policy: the case of the Arno River, Firenze, Italy. *Applied Geography, 34*, 205–218. http://dx.doi.org/10.1016/j.apgeog.2011.10.020.

Parcharidis, I., Foumelis, M., Kourkouli, P., & Wegmuller, U. (2009a). Persistent Scatterers InSAR to detect ground deformation over Rio-Antirio area (Western Greece) for the period 1992–2000. *Journal of Applied Geophysics, 68*(3), 348–355. http://dx.doi.org/10.1016/j.jappgeo.2009.02.005.

Parcharidis, I., Foumelis, M., Pavlopoulos, K., & Kourkouli, P. (2009b). Ground deformation monitoring in cultural heritage areas by time series interferometry: the case of ancient Olympia site (Western Greece). In *Proceeding of Fringe-ESA, Volume: European Space Agency, (Special Publication) ESA SP*.

PCN. (2014). *Ortofoto a colori anno 2008 con relative date del volo – Regioni Lazio e Umbria*. Available at http://www.pcn.minambiente.it/PCNDYN/catalogowms.jsp?lan=it. Last accessed 28.07.14.

Perissin, D., & Ferretti, A. (2007). Urban-target recognition by means of repeated spaceborne SAR images. *IEEE Transactions on Geoscience and Remote Sensing, 45*(12), 4043–4058.

Pratesi, F., Tapete, D., Terenzi, G., Del Ventisette, C., & Moretti, S. (2015). Structural assessment of case study historical and modern buildings in the Florentine area based on a PSI-driven seismic and hydrogeological risk analysis. In G. Lollino, D. Giordan, C. Marunteanu, B. Christaras, I. Yoshinori, & C. Margottini (Eds.), *Engineering geology for society and territory* (Vol. 5). Switzerland: Springer International Publishing. http://dx.doi.org/10.1007/978-3-319-09408-3_60.

Sciotti, M. (1982). Engineering geological problems due to old underground quarries in the urban area of Rome (Italy). In *IV International Congress International Association of Engineering Geology* (Vol. 1, pp. 211–225). New Delhi.

Sever, T. (2000). Remote sensing methods. In R. A. Williamson, & P. R. Nickens (Eds.), *Science and technology in historic preservation. Chapter discovery, documentation, and analysis* (p. 22).

Tapete, D., & Cigna, F. (2012a). Site-specific analysis of deformation patterns on archaeological heritage by satellite radar interferometry. In *20th International Materials Research Congress, Symposium 8 Cultural Heritage and Archaeological Issues in Materials Science, MRS Proceedings 1374* (pp. 283–295). Cambridge University Press. http://dx.doi.org/10.1557/opl.2012.1397.

Tapete, D., & Cigna, F. (2012b). Rapid mapping and deformation analysis over cultural heritage and rural sites based on persistent scatterer interferometry. *International Journal of Geophysics, 2012*. http://dx.doi.org/10.1155/2012/618609. Article ID 618609, 19 pp.

Tapete, D., & Casagli, F. (2013). Testing computational methods to identify deformation trends in RADARSAT persistent scatterers time series for structural assessment of archaeological heritage. In B. Murgante, S. Misra, M. Carlini, C. M. Torre, H-Q. Nguyen, & D. Taniar (Eds.), *ICCSA 2013, Part II, LNCS 7972* (pp. 693–707). Berlin Heidelberg: Springer-Verlag. http://dx.doi.org/10.1007/978-3-642-39643-4_50.

Tapete, D., Fanti, R., Cecchi, R., Petrangeli, P., & Casagli, N. (2012). Satellite radar interferometry for monitoring and early-stage warning of structural instability in archaeological sites. *Journal of Geophysics and Engineering, 9*(4), S10–S25. http://dx.doi.org/10.1088/1742-2132/9/4/S10.

Tapete, D., Fratini, F., Mazzei, B., Cantisani, E., & Pecchioni, E. (2013). Petrographic study of lime-based mortars and carbonate incrustation processes of mural paintings in Roman catacombs. *Periodico di Mineralogia, 82*(3), 503–527. http://dx.doi.org/10.2451/2013PM0030.

Tapete, D., Fratini, F., Mazzei, B., Cantisani, E., Riminesi, C., Manganelli Del Fà, R., et al. (2014). Methodological approach to monitor Roman catacombs: experience in the Catacombs of St Mark, Marcellian and Damasus, Rome, Italy. In C. Saiz-Jimenez (Ed.), *The conservation of subterranean cultural heritage* (pp. 51–58). CRC Press, ISBN 9781138026940.

TRE. (2010). *SqueeSAR™ – User manual*, 131 pp.

Ventriglia, U. (1971). *Geologia della Città di Roma*. Roma: Amministrazione Provinciale di Roma (in Italian).

Ventriglia, U. (2002). *Geologia del Territorio del Comune di Roma*. Amministrazione Provinciale di Roma–Difesa del Suolo, 809 pp. (in Italian).

Ventriglia, B., & Camponeschi, M. P. (1982). *Carta della Distribuzione delle Cave e delle Miniere, Regione Vulcanica dei Colli Albani, Provincia di Roma, Scala 1:100000*. Firenze: Litografia Artistica Cartografica.

Vinkler, A. P., Cashman, K., Giordano, G., & Groppelli, G. (2012). Evolution of the mafic Villa Senni caldera-forming eruption at Colli Albani volcano, Italy, indicated by textural analysis of juvenile fragments. *Journal of Volcanology and Geothermal Research, 235*, 37–54. http://dx.doi.org/10.1016/j.jvolgeores.2012.03.006.

Watkins, S. D., Giordano, G., Cas, R. A. F., & De Rita, D. (2002). Internal facies changes in mafic pyroclastic density current deposits: a record of temporal changes in the eruption style of the Villa Senni Eruption Unit, Alban Hills Volcano, Rome, Italy. *Journal of Volcanology and Geothermal Research, 118*, 173–204.

Witharana, C., Civco, D. L., & Meyer, T. H. (2013). Evaluation of pansharpening algorithms in support of earth observation based rapid-mapping workflows. *Applied Geography, 37*, 63–87.

Xu, X., & Min, X. (2013). Quantifying spatiotemporal patterns of urban expansion in China using remote sensing data. *Cities, 35*, 104–113.